But Mouse, you are not alone: On some severe acute respiratory syndrome coronavirus 2 variants infecting mice

Michael J. Kuiper, PhD, is a Biomolecular Modeller who leads the Modelling and Simulations Team in at the CSIRO Data61, Dockands, Victoria, Australia

Laurence OW Wilson, PhD, is a Research Scientist who leads the Digital Genome Engineering Team at the CSIRO Transformational Bioinformatics Group, North Ryde, New South Wales, Australia

Shruthi Mangalaganesh, is studying Bachelor of Biomedical Science and Bachelor of Commerce at Monash University, Clayton, Victoria, Australia, and pursued an internship at the CSIRO Australian Centre for Disease Preparedness, Geelong, Victoria, Australia

Carol Lee, BAnVetBioSci(Hons), PhD, is CERC Postdoctoral Research Fellow in the CSIRO Transformational Bioinformatics Group, North Ryde, New South Wales, Australia

Daniel Reti, BE(Hons), BS, worked as a Research Technician at the CSIRO Transformational Bioinformatics Group, North Ryde, New South Wales, Australia, and is currently Front-End Software Engineer at the Centre for Population Genomics, joint initiative of the Garvan Institute of Medical Research, Sydney, New South Wales, Australia and the Murdoch Children's Research Institute, Melbourne, Victoria, Australia

Seshadri S Vasan, DPhil, is a Senior Principal Research Consultant and COVID-19 Project Leader at the CSIRO Australian Centre for Disease Preparedness, Geelong, Victoria, Australia, and Honorary Professor in the Department of Health Sciences at the University of York, York, UK

Address correspondence to Professor Seshadri S Vasan, CSIRO Australian Centre for Disease Preparedness, 5 Portarlington Road, Geelong, 3220, Victoria, Australia or email vasan.vasan@csiro.au

NB: MJK and LOWW contributed equally to this paper.

Running Title: On some SARS-CoV-2 variants infecting mice

Abstract

In silico predictions combined with *in vitro*, *in vivo* and *in situ* observations collectively suggest that mouse adaptation of the SARS-CoV-2 virus requires an aromatic substitution in position 501 or position 498 (but not both) of the spike protein's receptor binding domain. This effect could be enhanced by mutations in positions 417, 484, and 493 (especially K417N, E484K, Q493K and Q493R), and to a lesser extent by mutations in positions 486 and 499 (such as F486L and P499T). Such enhancements due to more favourable binding interactions with residues on the complementary angiotensin-converting enzyme 2 (ACE2) interface, are however, unlikely to sustain mouse infectivity on their own based on

theoretical and experimental evidence to date. Our current understanding thus points to the Alpha, Beta and Gamma variants of concern infecting mice, while Delta and 'Delta Plus' lack a similar biomolecular basis to do so. This paper identifies eleven countries (Brazil, Chile, Djibouti, Haiti, Malawi, Mozambique, Reunion, Suriname, Trinidad and Tobago, Uruguay and Venezuela) where targeted local field surveillance of mice is encouraged because they may have come in contact with humans who had the virus with adaptive mutation(s). It also provides a systematic methodology to analyze the potential for other animal reservoirs and their likely locations.

Keywords

AlphaFold; Animal reservoir; COVID-19; *in silico*; *in vitro*; *in vivo*; mouse adaptation; SARS-CoV-2; variants

Introduction

The 'novel coronavirus disease' (COVID-19) has resulted in significant global morbidity and mortality on a scale similar to the influenza pandemic of 1918.[1] The ongoing pandemic has been sustained through the activities of human beings, who are the largest reservoir of the causative 'severe acute respiratory syndrome virus 2' (SARS-CoV-2). This RNA virus in a new host (human beings) is evolving rapidly, accumulating mutations, and existing as a cloud of variants with quasispecies diversity.[2] Last year, the world witnessed the risk of this virus acquiring additional reservoirs (such as minks) and new mutations of consequence (such as 'Cluster 5'), which could increase transmissibility and lead to a potentially weaker antibody response.[3]

Both the original form of the virus (known as 'D614') and the subsequent more transmissible 'G614' variant which has replaced it almost entirely in circulation,[4,5] did not infect mice because their 'angiotensin-converting enzyme 2' (ACE2) receptor did not bind the viral spike protein effectively to

60 allow entry into cells. Since mouse (*Mus musculus*) is a popular animal model of infection, the virus had
61 to be adapted through techniques such as sequential passaging in mouse lung tissues and modifying the
62 receptor binding domain (RBD).[6-8] Other strategies to infecting mice with the original form of the virus or
63 the G614 included transgenic mice expressing human ACE2 (hACE2), and sensitizing the mouse
64 respiratory tract through transduction with adenovirus or adeno-associated virus expressing hACE2.[9-12]
65 Recently, virus 'variants of concern' (VOC) originating from Brazil, South Africa and the UK (which
66 contain the common mutation N501Y in the RBD) were shown to infect mice.[13,14] This ability of SARS-
67 CoV-2 variants of concern to infect mice is unsettling because of the potential to establish additional
68 reservoirs in a species that is in close contact with people and companion animals, especially as its
69 population is hard to vaccinate or control.
70
71 **Methodology**
72 In this paper, we have combined our structural predictions from biomolecular modelling with available
73 experimental evidence to understand how specific mutations in VOC and mouse adapted strains,
74 especially in the RBD, have enabled this virus to infect mice. To do this, we compared the spatial
75 interactions of these key mutations with the corresponding regions in both mouse ACE2 (mACE2) and
76 hACE2 using homology molecular models based on cryogenic electron microscopy (cryo-EM) data of the
77 ACE2/RBD interface (protein database 'pdb' entry number 6M17).[15] We have assumed the coordinates
78 of ACE2 and RBD in the 6M17 structure to be reasonable starting positions for our respective models,
79 with root-mean-square deviation (RMSD) scripts alignment based on C-Alpha carbon protein backbones.
80 As the protein prediction software *AlphaFold* has been recently been released,[16] we also recalculated
81 RBD structures, finding *AlphaFold* predictions to be in excellent agreement with our initial homology
82 models, with less than 0.9 Å RMSD average alignment. Amino acid side chain conformations of the RBD
83 models were adapted from *AlphaFold* predictions as they were deemed more reliable.

84

85 By introducing the ACE2 models and variants into molecular dynamics simulations to optimize the
86 interactions, similar to our recent work,[17,18] we qualitatively identified the key interactions of side chain
87 residues at the ACE2/RBD interface. Further details are provided under 'Supplementary Methods for
88 Molecular Modelling'. We then compared our *in-silico* findings with experimental results reported by
89 different research groups with mouse adapted strains/isolates[6-8,13,21-29] and VOC[14,30-34] (**Tables 1 and 2**).
90 Taken together, we were able to gain valuable insights into the likely effects of different mutations of
91 consequence.

92

93 Subsequently, we queried the world's largest public database called 'GISAID' (Global Initiative on
94 Sharing All Influenza Data) and looked for these mutations, and equivalent mutations of consequence.
95 This 'Big Data', comprising of circa 2.4 million and 4 million SARS-CoV-2 genome sequences as of 21 July
96 and 4 October 2021 respectively, formed the basis of our *in situ* analysis.[29] Over 99.9% of these
97 sequences are from viruses sequenced from human hosts. In brief, sequences were aligned to the back
98 to the SARS-CoV-2 reference (EPI_ISL_402124, denoted as the WT allele) in order to generate a file
99 containing all mutations in the variant call format (VCF), which is a concise way for storing gene
100 sequence variations. We then calculated the ratio of the frequency at which the WT allele versus the
101 mutant allele were observed across a rolling 14-day window. Given the data is discrete, highly variable in
102 size across countries, and contains background noise, such a window of time is essential from our
103 experience to reduce distortions and glean meaningful insights. For example, if 14 WT and 28 mutant
104 sequences were observed within a specified 14-day window, then the frequencies were 1/day and 2/day
105 respectively. The ratio of mutant:WT frequency is therefore 2, indicating the mutant allele is appearing
106 twice as frequently as the WT allele within that period. This was used to create a heatmap for the key
107 mutations, both individually and in combination (as discussed below). For clarity, we only considered

108 countries where the mutant:WT ratio exceeded 1.2 across the entire time the mutant was sampled or
109 within any given 14-day window. To reduce the noise further from low-sampled countries, we also
110 instituted a minimum threshold of 10 WT and 10 mutant samples over at least 14 days to suggest
111 possible spread locally. For this reason, a country where a mutant had only been recorded on a single
112 day, or where only 9 mutant samples were recorded overall, was not included in our analysis. Our
113 heatmap scale has also been truncated at 2.00 for ease of visual comparison.
114
115 **Results and Discussion**
116 ***In silico* results**
117 *In silico* comparison of the interface residues of the RBD/ACE2 complex in human and mouse models
118 reveals 30 ACE2 residues in close contact, of which 19 are conserved between mACE2 and hACE2
119 (approximately 63% identity for the contacting ACE2 residues). The RBD mutations associated with the
120 mouse adaptations listed in **Table 1** can be grouped loosely into 3 regions by their positions on the
121 ACE2/RBD interface as follows: Region 1 (RBD positions 498, 499 and 501) are centered around the
122 highly conserved ACE2 residue tyrosine 41 (Y41); Region 2 (RBD positions 417, 493) centered around
123 ACE2 residue 34; and Region 3 (RBD positions 484 and 486) close to a cluster of ACE2 residues 78 to 82.
124 ACE2 residues within 5 Å (chosen to account for molecular fluctuations) of each RBD adaptation are
125 listed in **Table 3**, with dissimilar human/mouse ACE2 residues highlighted in yellow. **Figure 1** further
126 illustrates these residues visually, and how they are relatively positioned in three regions. **Figure 2** aligns
127 the human and mouse ACE2 to highlight the key differences at the contact points with the RDB (shown
128 in yellow).
129
130 Modelling the N501Y mutation at the ACE2/RBD interface reveals a close interaction with the highly
131 conserved Y41 residue in ACE2, through attractive, non-covalent bonding between aromatic amino acids

132 known as π-stacking interactions. In mACE2, π-stacking can be enhanced by the proximal substitution of
133 histidine (H) in place of lysine (K) which is present at position 353 of hACE2. Our modelling also shows
134 similar π-stacking enhancement with the conserved Y41, through the substitution of RBD glutamine at
135 position 498 (Q498) to either histidine (H) or tyrosine (Y). These aromatic π-stacking interactions appear
136 to be reasonably strong as N501Y and Q498H can each sustain mouse adaptation on its own in
137 experiments.[6,13,23,28] Counterintuitively, our modelling predicts that simultaneous aromatic mutations at
138 RBD positions 498 and 501 is detrimental to mouse adaptation due to local π-stacking distortion to the
139 binding interface. This could explain why very few simultaneous aromatic mutations at these positions
140 have been observed. In over 2.4 million entries on GISAID as of 21 July 2021, we detected only a single
141 co-occurrence, that of an adapted isolate from mouse lung homogenate where N501Y occurred with
142 glutamate 498 to arginine (Q498R).[29] However, when we recently re-run our *in situ* model with over 4
143 million human-origin GISAID entries, we detected 0, 2 and 14 instances of Y501 co-existing with Y498,
144 H498 and R498 respectively. The two instances of Y501-H498 are low quality and/or low coverage
145 sequences; the 14 instances of Y501-R498 have been reported from France, Netherlands, South Africa,
146 Spain, UK and USA between March and September 2021. Although arginine is not aromatic, it is
147 frequently associated with π-stacking interactions with inherent conformational flexibility compared to
148 tyrosine or histidine, therefore it is likely that the Y501-R498 combination is more tolerated.[37]
149
150 In Region 1 (**Table 3**) we also note the proline 499 to threonine (P499T) substitution in two infectious
151 clones, presumably engineered to enhance Y498. Modelling provides the following insight on this: the
152 change from P to T will relax the backbone constraints of proline and allow conformational
153 rearrangement of threonine to contact the conserved ACE2 residues Y41 and L45. However, we don't
154 find any strong molecular modelling basis for this mutation to sustain mouse adaptation on its own or
155 evolve naturally alongside adaptive mutations at positions 498 or 501; this is borne out by experimental

156 evidence to date. In other words, *in silico* predictions combined with *in vitro* and *in vivo* evidence
157 collectively suggest that mouse adaptation requires an aromatic substitution in either position 501 or
158 position 498 (but not both); while additional mutations, especially in Region 2 and Region 3 of the RBD
159 as summarized below, enhancing ACE2 binding interactions and specificity in mice. These predictions
160 are further supported by *AlphaFold* that assigns very high confidence scores (>93 in a scale of 0-100) for
161 the structural predictions involving these key mutations, demonstrating the applications of this
162 improved protein prediction software especially during pandemics such as COVID-19 and future
163 'Disease-X'.
164
165 From **Table 1**, we see that mouse adapted strains sometimes carry the Q493K/R mutation (polar
166 glutamine to basic lysine or arginine). Modelling predicts this as being enabled through favourable salt-
167 bridge interactions with both glutamic acid 35 (E35) or aspartic acid 38 (D38) both of which are
168 conserved in hACE2 as well as mACE2 (c.f. **Table 3**, Region 2). The K417N substitution (lysine to
169 asparagine), which is another experimental observation from **Table 1**, is also predicted by modelling to
170 be advantageous for mouse adaptation due to favourable amide hydrogen bond interactions with
171 interfacial mACE2 residues asparagine 31 (N31) and glutamine 34 (Q34); such amide hydrogen bonding
172 is not possible in hACE2 as it has non-amide lysine (K) and histidine (H) residues. With the Gamma
173 variant of concern, it is unclear whether the K417T enhances the role of N501Y in mouse adaptation in a
174 similar manner. The 'Delta Plus' variant of concern has the K417N mutation, but there is no molecular
175 modelling basis to believe that it can infect mice without an aromatic change in position 498 or 501 as
176 described above. It would be worthwhile to further investigate any interfering role of glycosylation at
177 this interface region, because hACE2 contains N-linked glycosylation at asparagine 90 (N90) whereas
178 mACE2 does not (its analogous residue is threonine T90 according to Uniprot references Q8R0I0 and
179 Q9BYF1).

180

181 In Region 3, the K484 residue is not positioned directly at the interface and not observed to interact
182 strongly with any ACE2 residues; however, our model shows occasional salt bridges can be formed with
183 relatively close glutamic acid residues in positions 35 and 75 that are conserved in both hACE2 and
184 mACE2. Our simulations show that the distance between K484 and these glutamic acid residues
185 fluctuate dynamically from 3 to 20 Å, with salt bridges more likely when distances are around 3 Å. Thus,
186 the E484K, which is present in the Beta and Gamma variants of concern, and more recently in some
187 Alpha isolates as well, is likely to have an enhancing role through transient salt bridges. The same cannot
188 be said about E484Q seen in the Delta variant of concern because salt bridge formation is unlikely with
189 the polar glutamine (Q) residue. With no accompanying aromatic change in positions 498 or 501, we
190 believe that the E484Q in Delta, and additionally the K417N in 'Delta Plus', cannot sustain mouse
191 infectivity on their own based on current biomolecular understanding. The residues 75 to 82 in mACE2
192 are significantly different from hACE2 (**Table 3**), therefore any mutation in the corresponding RBD
193 interface is worth investigation. We could find one from experimental observations, the engineered
194 substitution F486L,[27] and consider it to have at best an enhancing role. As it was observed
195 simultaneously with Q498Y (which is likely to sustain mouse infectivity on its own), the contribution of
196 F486L to the overall mouse adaptation remains to be ascertained.

197

198 **Comparison with *in vitro, in vivo* and *in situ* observations**

199 Early *in silico* predictions based on comparative structural analysis of ACE2 suggested that mouse has a
200 very low probability of being infected.[35,36] Although correct about mouse, those analyses also made
201 inconsistent and erroneous predictions that ferrets wouldn't be susceptible, pigs would be susceptible,
202 etc., thus exposing the need for experimental inputs into the model. Therefore, this paper takes into
203 account a range of experimental observations to cross-check our *in silico* predictions through

204 biomolecular modelling. Wan *et al.* reasoned that "*mouse or rat ACE2 contains a histidine at the 353*
205 *position which does not fit into the virus-receptor interaction as well as a lysine does*". [35] While this is
206 true of the original Wuhan strain containing asparagine 501 (N501) in the RBD, our modelling indicates
207 why the tyrosine 501 mutation enables mouse infectivity, even on its own. In hACE2, lysine 353 (K353)
208 creates a salt bridge with conserved aspartic acid 38 (D38). In mACE2, lysine 353 is replaced by the
209 aromatic histidine (H353) to complete the salt bridge, as well as contribute to π-stacking with Y501
210 variant. The N501Y mutation will also lead to favorable π-stacking with the highly conserved tyrosine 41
211 (Y41) residue in mammalian ACE2, as suggested by Starr *et al.*[38] with deep scanning of RBD mutations
212 and hACE2 affinity assays. These authors highlighted enhanced affinity of F501 (as it had the highest
213 score), followed by Y501, V501, W501 and T501, in that order. But Y501 and T501 require only a single
214 nucleotide change and have been observed more frequently *in situ* (**Figure S1a**) – compared to F501,
215 V501 and W501 which require 2, 2 and 3 nucleotide changes respectively. It is unsurprising that the
216 latter variants requiring two or more changes were rarely observed *in situ* regardless of their high *in*
217 *vitro* affinity scores from Starr *et al.*[38]
218
219 From the above and **Table 4**, we see that *in silico* analysis can provide valuable insights to interpret and
220 bridge *in vitro*, *in vivo* and *in situ* observations on the RBD position 501. A similar analysis is possible with
221 the alternative essential mutation for mouse adaptation at RBD position 498, where the *in vitro* affinity
222 enhancement order is H498, Y498, F498 and W498 according to Starr *et al.*[38] Of these, H498 (on its own)
223 and Y498 (with enhancing RBD mutations) have been shown to result in mouse adaptation *in vivo* (**Table**
224 **1**);[7,8,23-28] Q498R was also reported once, unusually in combination with N501Y, isolated from mouse
225 lung after 30 passages. In humans, *in situ* observations of these variants have been limited to R498 (57
226 occurrences) and H498 (8 occurrences) so far. Thus, it is clear from *in vitro*, *in vivo* and *in situ* analyses
227 (**Table 4**) that H498, R498 and Y498 are possible but not yet common. This is consistent with our *in silico*

228 predictions because H498 and Y498 are aromatic (enabling π-stacking with ACE2 Y41; similar to Y501),
229 while R498 has conformational flexibility and can still be associated with π-stacking interactions.[37] H498
230 and R498 observed *in situ* require a single nucleotide change from Q498, while Y498 requires two
231 nucleotide changes (or one change from H498).
232
233 Similar insights are also possible for the enhancing RBD mutations (c.f. **Table 1** and **Table 4**). From *in vivo*
234 and *in situ* observations, we see that K417M is less common than K417N or K417T (**Figures S2a** and **S2b**),
235 although *in vitro* studies did not predict any enhancement.[38] *In silico* predictions show that all these
236 require a single nucleotide change, but that N417 (and Q417) would benefit from amide hydrogen
237 bonding. E484K is present in Beta and Gamma (**Figure S2c**), and increasingly in Alpha VOC, while E484Q
238 is present in the Kappa variant of interest that is related to the Delta VOC. In comparison to these two
239 substitutions and notwithstanding higher *in vitro* affinity scores, R484 and T484 are infrequently
240 observed *in situ*, which is consistent with our *in silico* predictions because they each require 2 nucleotide
241 changes from E484, or one change from K484. The F486L and P499T were originally engineered *in vivo*,
242 but have had sporadic *in situ* presence in human populations. *In silico* predictions suggest that the F486L
243 mutation (accessible by three possible ways of a single nucleotide change) can aid mACE2 adaptation,
244 due to the human-mouse differences in ACE2 at the 78-82 region; the P499T is also a single nucleotide
245 change (but only one way from P to T) and predicted to be rare in comparison. Finally, *in silico*
246 predictions for Q493 substituted by K, L or R (each a single nucleotide change) are borne out *in vivo* and
247 *in situ*, although their affinity scores from *in vitro* experiments are low. The affinity scores from Starr *et*
248 *al.*[38] were developed for hACE2 (not mACE2), so we expected a greater correlation than what has been
249 observed *in situ* in human populations, but perhaps it is still early in the pandemic to assess this
250 definitively. It also looks likely that there are factors other than enhancement of ACE2 binding that
251 determine susceptibility – as seen from Starr *et al.*[38] and **Table 4**; from our own inconclusive attempts at

correlating free energy binding affinities using *in silico* methods (not shown); and from a more detailed *in silico* model by Piplani *et al.*[39] which counter-intuitively predicts lower binding free energy for dogs compared to more susceptible animals such as monkeys, hamsters, ferrets, cats and tigers.[40]

Some mutations in the essential as well as enhancing positions can lead to other mutations. For example, N501Y, the key mutation common to the Alpha, Beta, and Gamma variants of concern, can lead to F501 with a further nucleotide change. Similarly, the enhancing E484K mutation can also lead to R484 or T484 with a further nucleotide change. We examined whether *in situ* observations are consistent or contrary to our *in silico* predictions. Indeed, F501 was observed in Sweden (28 April 2021), Germany (7 May 2021), Mexico (22 June 2021) and Colombia (30 June 2021), once in each of these four countries, while the Y501 has been observed in these countries since 12 March 2020, 21 October 2020, 31 January 2021 and 19 September 2020 respectively. UK reported E484R in August 2020, followed by Angola in April 2021; Brazil and USA in May 2021; South Korea in June 2021; and South Africa in July 2021. In each case, the E484K was detected prior to E484R – the former mutation circulating in UK, Angola, Brazil, USA, South Korea and South Africa from April, August, April, March, December and August 2020 respectively. Similarly, E484T was only recently detected in the USA in June 2021, 15 months after the first report of E484K in that country. All eleven instances are thus consistent with our prediction – whether this link is causal or a coincidence is worthy of investigation with local epidemiological data. While bioinformatics tools can provide useful insights, out of 53 COVID-positive cases only one sample is on average sent for virus genome sequencing (as of 4 October 2021), with huge variations across time and locations, and lots of missing meta-data.[41,42] This means we are more confident about ruling in (e.g. when a variant has been detected in a location) than ruling out the possibility of a mutation circulating purely based on *in silico* data, even if the latter is statistically large (4 million as of 4 October 2021).

276

277 Our analysis is not just of theoretical interest; it has huge practical applications because mice can be
278 kept as pets, or come into contact with other pets like cats which are known to be susceptible. Also,
279 mouse plague can occur in area of COVID-19 outbreaks or endemicity, as is currently the case in New
280 South Wales and adjacent states of Australia.[43] In order to help public health and animal health
281 professionals, Figures 3a and 3b show the eleven countries where key essential and enhancing
282 mutations listed in Tables 1 and 4 (viz. N501Y, E484K and K417N/T) have co-occurred. Supplementary
283 Table S1 gives the raw data, down to regional counts for these combinations. We believe that this
284 information will help locate areas at risk (especially in Brazil, Chile, Djibouti, Haiti, Malawi, Mozambique,
285 Reunion, Suriname, Trinidad and Tobago, Uruguay and Venezuela) for appropriate mitigation measures.

286

287 **Conclusion and further analyses**

288 Assessing the risk of viruses adapting to new hosts requires careful interpretation of all available data
289 from *in silico*, *in vivo*, *in vitro* and *in situ* sources. Understanding host adaptation at a molecular level, via
290 modelling helps reconcile seemingly conflicting, experimental, and clinical observations while a
291 pandemic is still in progress. We have demonstrated this with the SARS-CoV-2 virus adapting to mice.
292 Our conclusions come with humility, as they are based on best available evidence up to this point, but
293 allowing us and others to refine when more evidence becomes available. Armed with our collective
294 understanding from different approaches, and bolstered by bioinformatics and emerging artificial
295 intelligence technologies such as *AlphaFold*, we have shown how to position ourselves better to predict
296 and mitigate virus host adaptations, not just for this pandemic but also for future Disease-X. Further
297 analyses pertaining to COVID-19 should focus on the role of mutations beyond the spike and RBD;
298 improved computational modelling of binding affinities to explore correlations with susceptibility, if any;

299 and study other hosts like rats and other potential reservoir species (even those that previously
300 exhibited low receptor activities) which will be hard to vaccinate or control.[35,36,44]
301
302 **Supplementary Methods for Molecular Modelling**
303 Molecular simulations were performed using NAMD2.14[45] with CHARM36m[46] forcefield employing a
304 'TIP3' water model. The SARS-CoV-2 spike/ACE2 model was a homology model based on
305 the pdb structure 6M17.[15] Variant models of the SARS-CoV-2 spike RBD domain (residues 330 to 530)
306 containing the mouse adapted mutations were constructed by mutating residues in the NAMD build
307 scripts, but later found to be in very close agreement with the same model constructed using
308 *AlphaFold*[16] (less than 0.9 Å RMSD difference to C-Alpha backbone atoms). A truncated mACE2
309 consisting of residues 19 to 600 was built using Swiss modeller,[47] and similarly found to be in close
310 agreement with the equivalent *AlphaFold* model. Amino acid side chain conformations predicted by
311 *AlphaFold* were used in all initial RBD model starting conformations. Glycosylation of the spike and
312 mACE2 protein was manually constructed using Visual Molecular Dynamics (VMD). Simulations were
313 run with Periodic Boundary Conditions 'PBCs' using the 'NPT' isothermal-isobaric ensemble at 310K and
314 1 bar pressure employing Langevin dynamics. The PBCs were constant in the XY dimensions. Long-range
315 Coulomb forces were computed with the Particle Mesh Ewald method with a grid spacing of 1 Å. 2 fs
316 timesteps were used with non-bonded interactions calculated every 2 fs and full electrostatics every 4 fs
317 while hydrogens were constrained with the 'SHAKE' algorithm. The cut-off distance was 12 Å with a
318 switching distance of 10 Å and a pair-list distance of 14 Å. Pressure was controlled to 1 atmosphere
319 using the Nosé-Hoover Langevin piston method employing a piston period of 100 fs and a piston decay
320 of 50 fs. Trajectory frames were captured every 100 ps. Eleven variant models were constructed
321 representing the mouse-adapted variants observed in **Table 1** as well as the original Wuhan RBD model
322 with both mouse and human ACE2. Models were simulated for 300 nanoseconds. Trajectories were

visualized with VMD and Nanome. Modelling data shall be made available on the CSIRO Data access portal (https://data.csiro.au/).

Acknowledgements

This work was supported by funding (Principal Investigator: S.S.V.) from the Australia's Department of Finance, CSIRO Future Science Platforms, National Health and Medical Research Council (MRF2009092), and United States Food and Drug Administration (FDA) Medical Countermeasures Initiative contract (75F40121C00144). The article reflects the views of the authors and does not represent the views or policies of the funding agencies including the FDA. We are grateful for support from our colleagues at the Australian Centre for Disease Preparedness (https://www.grid.ac/institutes/grid.413322.5) (especially Simran Chahal, Trevor Drew, Alexander McAuley and Nagendrakumar Singanallur) and the Transformational Bioinformatics Group (especially Denis Bauer, Yatish Jain, Brendan Hosking and Aidan Tay). The title is from the poem '*To a Mouse: On Turning her up in her Nest, with the Plough, November 1785*' by Scotland's national poet Robert Burns, in which he says that the mouse is not alone in proving foresight may be vain as the best-laid schemes of mice and men go oft awry (*But, Mousie, thou art no thy-lane, In proving foresight may be vain: The best-laid schemes o' Mice an' Men Gang aft agley*).

Author contributions

Conceptualization, methodology, and funding acquisition, S.S.V.; *in silico* analysis, M.J.K.; *in vitro* analysis, M.J.K. and S.S.V.; *in vivo* analysis, S.M. and S.S.V.; *in situ* analysis, L.O.W.W., D.R. and C.L.; writing – original draft preparation, S.S.V, M.J.K. and S.M.; writing – review and editing, all authors.

References

346 1. Dong E, Du H, Gardern L. An interactive web-based dashboard to track COVID-19 in real time.
347 *Lancet Infectious Diseases.* 2020;20(5):533-534. Available at https://doi.org/10.1016/S1473-
348 3099(20)30120-1 (accessed 1 December 2020).
349 2. Bauer DC, Tay AP, Wilson, LOW, et al. Supporting pandemic response using genomics and
350 bioinformatics: A case study on the emergent SARS-CoV-2 outbreak. *Transboundary & Emerging*
351 *Diseases*. 2020; 67(4):1453-1462. Available at https://doi.org/10.1111/tbed.13588 (accessed 1
352 December 2020).
353 3. Lassaunière R, Fonager J, Rasmussen, M, et al. Working paper on SARS-CoV-2 spike mutations
354 arising in Danish mink, their spread to humans and neutralization data. 2020. Available at
355 https://files.ssi.dk/Mink-cluster-5-short-report_AFO2 (accessed 1 December 2020).
356 4. Korber B, Fischer WM, Gnanakaran S, et al. Tracking changes in SARS-CoV-2 spike: Evidence that
357 D614G increases infectivity of the COVID-19 virus. *Cell*. 2020; 182(4):812-827. Available at
358 https://doi.org/10.1016/j.cell.2020.06.043 (accessed 1 December 2020).
359 5. Zhang J, Cai Y, Xiao T, et al. Structural impact on SARS-CoV-2 spike protein by D614G
360 substitution. *Science*. 2021; 372(6541):525-530. Available at
361 https://doi.org/10.1126/science.abf2303 (accessed 1 May 2021).
362 6. Gu H, Chen Q, Yang G, et al. Adaptation of SARS-CoV-2 in BALB/c mice for testing vaccine
363 efficacy. *Science*. 2020; 369(6511):1603-1607. Available at
364 https://doi.org/10.1126/science.abc4730 and
365 https://www.biorxiv.org/content/10.1101/2020.05.02.073411v1 (accessed 1 December 2020).
366 7. Dinnon KH, Leist SR, Schäfer A, et al. A mouse-adapted model of SARS-CoV-2 to test COVID-19
367 countermeasures. *Nature*. 2020; 586:560-566. Available at https://doi.org/10.1038/s41586-020-
368 2708-8 (accessed 1 December 2020).

369 8. Leist SR, Dinnon KH, Schäfer A, et al. A mouse-adapted SARS-CoV-2 induces acute lung injury
370 and mortality in standard laboratory mice. *Cell*. 2020; 183:1070-1085. Available at
371 https://doi.org/10.1016/j.cell.2020.09.050 (accessed 1 December 2020).
372 9. Yuan L, Tang Q, Cheng T, Xia N. Animal models for emerging coronavirus: progress and new
373 insights. *Emerging Microbes & Infections*. 2020; 9(1):949-961. Available at
374 https://doi.org/10.1080/22221751.2020.1764871 (accessed 15 May 2021).
375 10. Muñoz-Fontela C, Dowling WE, Funnell SGP, et al. Animal models for COVID-19. *Nature*. 2020;
376 586: 509-515. Available at https://doi.org/10.1038/s41586-020-2787-6 (accessed 1 December
377 2020).
378 11. Zeiss CJ, Compton S, Veenhuis, RT. Animal models of COVID-19. I. Comparative virology and
379 disease pathogenesis. *ILAR Journal*. 2021; ilab007. Available at
380 https://doi.org/10.1093/ilar/ilab007 (accessed 1 May 2021).
381 12. Veenhuis RT, Zeiss CJ. Animal models of COVID-19 II. Comparative immunology. *ILAR Journal*.
382 2021; ilab010. Available at https://doi.org/10.1093/ilar/ilab010 (accessed 1 May 2021).
383 13. Rathnasinghe R, Jangra S, Cupic A, et al. The N501Y mutation in SARS-CoV-2 spike leads to
384 morbidity in obese and aged mice and is neutralized by convalescent and post-vaccination
385 human sera. *medRxiv*. 2021; 2021.01.19.21249592. Available at
386 https://doi.org/10.1101/2021.01.19.21249592 (accessed 1 February 2021).
387 14. Yao W, Wang Y, Ma D, et al. Circulating SARS-CoV-2 variants B.1.1.7, 501Y.V2, and P.1 have
388 gained ability to utilize rat and mouse Ace2 and altered in vitro sensitivity to neutralizing
389 antibodies and ACE2-Ig. *bioRxiv*. 2021; 2021.01.27.428353. Available at
390 https://doi.org/10.1101/2021.01.27.428353 (accessed 1 May 2021).

391 15. Yan R, Zhang Y, Li Y, et al. Structural basis for the recognition of SARS-CoV-2 by full-length
392 human ACE2. *Science*. 2020; 367:1444-1448. Available at
393 https://doi.org/10.1126/science.abb2762 (accessed 1 December 2020).
394 16. Jumper, J., Evans, R., Pritzel, A. *et al.* Highly accurate protein structure prediction with
395 *AlphaFold*. *Nature* (2021). Available at https://doi.org/10.1038/s41586-021-03819-2 (accessed
396 20 July 2021).
397 17. McAuley AJ, Kuiper MJ, Durr PA, et al. Experimental and *in silico* evidence suggests vaccines are
398 unlikely to be affected by D614G mutation in SARS-CoV-2 spike protein. *Npj Vaccines*. 2020;
399 5:96. Available at https://doi.org/10.1038/s41541-020-00246-8 (accessed 1 December 2020).
400 18. Riddell S, Goldie S, McAuley A, et al. Live virus neutralisation of the 501Y.V1 and 501Y.V2 SARS-
401 CoV-2 variants following INO-4800 vaccination of ferrets. *bioRxiv*. 2021; 2021.04.17.440246.
402 Available at https://doi.org/10.1101/2021.04.17.440246 (accessed 1 May 2021).
403 19. Tai W, He L, Zhang X. Characterization of the receptor-binding domain (RBD) of 2019 novel
404 coronavirus: implication for development of RBD protein as a viral attachment inhibitor and
405 vaccine. Cellular & Molecular Immunology. 2020; 17:613-620. Available at
406 https://doi.org/10.1038/s41423-020-0400-4 (accessed 1 December 2020).
407 20. Grantham, R. Amino acid difference formula to help explain protein evolution. *Science*. 1974;
408 185(4154): 862-864. Available at https://doi.org/10.1126/science.185.4154.862 (accessed 1
409 December 2020).
410 21. Sun S, Gu H, Cao L, et al. Characterization and structural basis of a lethal mouse-adapted SARS-
411 CoV-2. bioRxiv. 2020; 2020.11.10.377333. Available at
412 https://doi.org/10.1101/2020.11.10.377333 (accessed 1 December 2020).

413 22. Fagre A, Lewis J, Eckley M, et al. SARS-CoV-2 infection, neuropathogenesis and transmission
414 among deer mice: Implications for spillback to New World rodents. *PloS Pathogens*. 2021; 17(5):
415 e1009585. Available at https://doi.org/10.1371/journal.ppat.1009585 (accessed 24 May 2021).
416 23. Wang J, Shuai L, Wang C, et al. Mouse-adapted SARS-CoV-2 replicates efficiently in the upper
417 and lower respiratory tract of BALB/c and C57BL/6J mice. *Protein & Cell*. 2020; 11:776-782.
418 Available at https://doi.org/10.1007/s13238-020-00767-x (accessed 1 December 2020).
419 24. Liu Z, Zheng H, Lin H, et al. Identification of common deletions in the spike protein of Severe
420 Acute Respiratory Syndrome Coronavirus 2. *Journal of Virology.* 2020; 94(17):e00790-20.
421 Available at https://doi.org/10.1128/JVI.00790-20 (accessed 1 December 2020).
422 25. Zhou H, Chen X, Hu T, et al. A novel bat coronavirus closely related to SARS-CoV-2 contains
423 natural insertions at the S1/S2 cleavage site of the spike protein. *Current Biology.* 2020;
424 30:2196-2203. Available at https://doi.org/10.1016/j.cub.2020.05.023 (accessed 1 December
425 2020).
426 26. Huang K, Zhang Y, Hui X, et al. Q493K and Q498H substitutions in spike promote adaptation of
427 SARS-CoV-2 in mice. *EbioMedicine*. 2021; 67:103381. Available at
428 https://doi.org/10.1016/j.ebiom.2021.103381 (accessed 24 May 2021).
429 27. Muruato A, Vu MN, Johnson BA, et al. Mouse adapted SARS-CoV-2 protects animals from lethal
430 SARS-CoV challenge. *bioRxiv.* 2021; 2021.05.03.442357. Available at
431 https://doi.org/10.1101/2021.05.03.442357 (accessed 15 May 2021).
432 28. Zhang Y, Huang K, Wang T, et al. SARS-CoV-2 rapidly adapts in aged BALB/c mice and induces
433 typical pneumonia. *Journal of Virology*. 2021; 95(11):e02477-20. Available at
434 https://doi.org/10.1128/JVI.02477-20 (accessed 24 May 2021).

435 29. Van Noorden, R. Scientists call for fully open sharing of coronavirus genome data. *Nature*. 2021;
436 590:195-196. Available at https://doi.org/10.1038/d41586-021-00305-7 (accessed 1 March
437 2021).
438 30. Rambaut A, Loman N, Pybus O, et al. Preliminary genomic characterisation of an emergent
439 SARS-CoV-2 lineage in the UK defined by a novel set of spike mutations. *Virological*. 2020.
440 Available at https://virological.org/t/preliminary-genomic-characterisation-of-an-emergent-sars-
441 cov-2-lineage-in-the-uk-defined-by-a-novel-set-of-spike-mutations/563 (accessed 1 March
442 2021).
443 31. Li Q, Nie J, Wu J, et al. SARS-CoV-2 501Y.V2 variants lack higher infectivity but do have immune
444 escape. *Cell.* 2021; 184(9):2362-2371. Available at https://doi.org/10.1016/j.cell.2021.02.042
445 (accessed 1 May 2021).
446 32. Montagutelli X, Prot M, Levillayer L, et al. The B1.351 and P.1 variants extend SARS-CoV-2 host
447 range to mice. *bioRxiv.* 2021; 2021.03.18.436013. Available at
448 https://doi.org/10.1101/2021.03.18.436013 (accessed 1 May 2021).
449 33. Faria NR, Claro IM, Candido D, et al. Genomic characterisation of an emergent SARS-CoV-2
450 lineage in Manaus: preliminary findings. *Virological*. 2021. Available at
451 https://virological.org/t/genomic-characterisation-of-an-emergent-sars-cov-2-lineage-in-
452 manaus-preliminary-findings/586 (accessed 1 March 2021).
453 34. Lucaci AG, Zehr JD, Shank SD, et al. RASCL: Rapid assessment of SARS-COV-2 clades enabled
454 through molecular sequence analysis and its application to B.1.617.1 and B.1.617.2. *Virological*.
455 2021. Available at https://virological.org/t/rascl-rapid-assessment-of-sars-cov-2-clades-enabled-
456 through-molecular-sequence-analysis-and-its-application-to-b-1-617-1-and-b-1-617-2/709
457 (accessed 29 May 2021).

458 35. Wan Y, Shang J, Graham R, et al. Receptor recognition by novel coronavirus from Wuhan: an
459 analysis based on decade-long structural studies of SARS coronavirus. *Journal of Virology.* 2020;
460 94(7):e00127-20. Available at https://doi.org/10.1128/JVI.00127-20 (accessed on 1 December
461 2020).
462 36. Damas J, Hughes GM, Keough C, et al. Broad host range of SARS-CoV-2 predicted by comparative
463 and structural analysis of ACE2 in vertebrates. *PNAS.* 2020; 117(36):22311-22322. Available at
464 https://doi.org/10.1073/pnas.2010146117 (accessed 1 December 2020).
465 37. Flocco MM, Mowbray SL. Planar stacking interactions of arginine and aromatic side-chains in
466 proteins. *Journal of Molecular Biology*. 1994; 235(2):709-717. Available at
467 https://doi.org/10.1006/jmbi.1994.1022 (accessed 1 December 2020).
468 38. Starr TN, Greaney AJ, Hilton SK, et al. Deep mutational scanning of SARS-CoV-2 receptor binding
469 domain reveals constraints on folding and ACE2 binding. *Cell*. 2020; 182(5):1295-1310.e20.
470 Available at https://doi.org/10.1016/j.cell.2020.08.012 (accessed 1 December 2020).
471 39. Piplani S, Singh PK, Winkler DA, Petrovsky, N. *In silico* comparison of SARS-CoV-2 spike protein-
472 ACE2 binding affinities across species and implications for virus origin. *Scientific Reports.* 2021;
473 11:13063. Available at https://doi.org/10.1038/s41598-021-92388-5 (accessed 1 October 2021).
474 40. Muñoz-Fontela C, Dowling, WE, Funnell, SGP, et al. Animal models for COVID-19. *Nature.* 2020;
475 586:509-515. Available at https://doi.org/10.1038/s41586-020-2787-6 (accessed 1 December
476 2020).
477 41. Bauer DC, Metke-Jimenez A, Maurer-Stroh S, et al. Interoperable medical data: the missing link
478 for understanding COVID-19. *Transboundary & Emerging Diseases*. 2021; 68(4):1753-1760.
479 Available at https://onlinelibrary.wiley.com/doi/10.1111/tbed.13892 (accessed 1 July 2021).
480 42. Priyadarshini, S. Massive coronavirus sequencing efforts urgently need patient data. *Nature*
481 *India (special issue #13 on COVID-19 crisis)*. 2020; 10.1038/nindia.2020.75:11-13. Available at

482 https://www.natureasia.com/en/nindia/pdf/special-issues/13/Nature-India-COVID-19-Crisis.pdf
483 and https://go.nature.com/2y7kUIw (accessed 1 December 2020).
484 43. NSW Government. Help for regional communities impacted by the mouse plague. 2021.
485 Available at https://www.nsw.gov.au/initiative/mouse-control-support-program (accessed 24
486 May 2021).
487 44. Zhao X, Chen D, Szabla R, et al. Broad and differential animal angiotensin-converting enzyme 2
488 receptor usage by SARS-CoV-2. *Journal of Virology*. 2020; 94(18):e00940-20. Available at
489 https://doi.org/10.1128/JVI.00940-20 (accessed 1 December 2020).
490 45. Phillips JC, Braun R, Wang W, et al. Scalable molecular dynamics with NAMD. *Journal of*
491 *Computational Chemistry*. 2005; 26:1781-1802. Available at https://doi.org/10.1002/jcc.20289
492 (accessed 1 December 2020).
493 46. Huang J, Rauscher S, Nawrocki G, et al. CHARMM36m: an improved force field for folded and
494 intrinsically disordered proteins. *Nature Methods.* 2017; 14:71-73. Available at:
495 https://doi:10.1038/nmeth.4067 (accessed 1 December 2020).
496 47. Waterhouse A, Bertoni M, Bienert S, et al. SWISS-MODEL: homology modelling of protein
497 structures and complexes. *Nucleic Acids Research*. 2018; 46:W296-W303. Available at
498 https://doi.org/10.1093/nar/gky427 (accessed 1 December 2020).
499

Mice-infecting SARS-CoV-2 'strains'/isolates	Key mutations in the spike RBD (residues 331-524)[19]							Color legend – mutations scored on Grantham Distance,[20] in the scale of 5 (conservative) to 215 (radical), similar to Riddell et al.[18]										
	K417	E484	F486	Q493	Q498	P499	N501	22	24	38	43	53	56	73	94	95	99	143
Mouse Adapted (MA) strains								**Authors' synthesis/comments**										
MASCp6[6]							N→Y	L37F (nsp6), P84S (nsp10), and D128Y (N) were the other observed nonsynonymous mutations.										
MASCp25[21]				Q→K			N→Y	MASCp6 passaged serially to develop MASCp25 and MASCp36, which accumulated Q493K and subsequently K417N in the RBD.										
MASCp36[21]	K→N			Q→K			N→Y	Highly virulent in aged mice and reported stable/mature RBD binding. It also had I1258V (nsp3), S301L (nsp5), and R32C (N).										
IC-MA1[7]					Q→Y	P→T		Spike Q498Y and P499T were engineered for compatibility with Q42 of mouse ACE2.										
IC-MA10[8]				Q→K	Q→Y	P→T		Q493K evolved in MA10 and interacts with mACE2's N31; others were T285I (nsp4), K2R (nsp7), E23G (nsp8), and F7S (ORF6).										
WA1-MA-P11[13]							N→Y	In addition to N501Y, there were H655Y, T7I (M), L84S (ORF8), S194T (N) and the +KLRS (216-219) insertion also observed by others and predicted to form a solvent-accessible loop.[22]										
HRB26M[23] (HRB26-P14)					Q→H			HRB26-P5 had Q498H, N969S, and the 675QTQTN679 deletion observed by others.[24,25] P14 also had A81T (nsp8).										
Hu-1-WBP-1[26]				Q→K	Q→H			Q493K and Q498H by P5, interacting respectively with mACE2's N31 via H-bond and Y41 via π-stacking. Nonsynonymous Q493K and T77I (nsp9) mutations increased frequency from P8 to P11.										
IC-MA4[27]			F→L		Q→Y			F486L and Q498Y were engineered for infecting mice.										
IC-CMA1-3[27]	K→N						N→Y	CMA1-3 all had N501Y. CMA2 also had D128Y; CMA3 also had D128Y, L37F, and P87S. Passaging of CMA3 resulted in K417N, H655Y, and E8V (E).										
LG[28]					Q→H			Other mutations present were N74K, H655Y, I6V (ORF10).										
IA-N501Y-MA30	K→M	E→K		Q→R	Q→R		N→Y	Homogenate from BALB/c mouse lung after 30 passages. GISAID entry EPI_ISL_1666328.[29]										
Variants of Concern (VOC) infecting mice																		
Alpha (501Y.V1 or B.1.1.7[14,30])		E→K					N→Y	First reported in the UK, September 2020. Spike also has A570D, P681H, T716I, S982A, and D1118H, in addition to HV69-70 and Y144 deletions. **E484K has been detected in this VOC in 15 countries as of 29 April 2021 (436 entries on GISAID).**										
Beta (501Y.V2 or B.1.351[14,31,32])	K→N	E→K					N→Y	First reported in South Africa, May 2020. V2-1 had D80A, D215G, E484K, N501Y, D614G and A701V in the Spike. L18F and K417N arose in V2-2. V2-3 had 242-244 deletion.										
Gamma (501Y.V3 or P.1[14,32,33])	K→T	E→K					N→Y	First reported in Brazil, November 2020. L18F, T20N, P26S, D138Y, R190S, K417T, E484K, N501Y, H655Y and T1027I in Spike.										
VOC not known to infect mice																		
Delta (452R.V3 or B.1.617.2)[34]	K→N							First reported in India, October 2020. Also has L452R in the RBD; G142D, R158G, T478K, P681R and D950N in Spike, along with deletions 156-157. **K417N has been detected in this VOC (called 'Delta Plus') in 12 countries as of 25 June 2021.** The related Kappa variant of interest (B.1.617.1) has L452R and E484Q in RBD (Grantham Distance scores of 102 and 29 respectively).										

Table 1 Key mutations in 14 'mouse adapted strains' and 3 'variants of concern' of SARS-CoV-2 known to infect mice, with further characterization as outlined in **Table 2**.

Species and age of mice (Study reference)	Strain, dose, shedding and transmission*	Evidence of productive SARS-CoV-2 replication in the respiratory tract	Clinical outcomes, histopathological evidence of disease
Aged (9 months old) and young (6 weeks old) BALB/c mice studied. (Gu et al, 2020)[6]	**Strain name:** MASCp6 **Dose:** Intranasal inoculation with 1.6×10^4 PFU **Shedding**: Viral shedding observed in the feces at day 3,5 and 7 after inoculation. **Transmission**: No information	High amounts of viral RNAs in the lungs and tracheas were detected at 3, 5 and 7 days after inoculation in all aged mice, with peak viral RNA loads of ~10^{10} copies/g at 3 days after inoculation. Viral RNAs were also detected in heart, liver, spleen, and brain. Similar tissue distribution of SARS-CoV-2 RNA was also seen in the MASCp6 infected young mice.	**Clinical:** No visible clinical symptoms or body weight loss were observed in both the young and aged mice. No fatalities recorded. **Histopathological:** Led to interstitial pneumonia and inflammatory responses in both young and aged mice, however the lung damage in the aged mice was more severe.
Young (8-week-old) and aged (9 months old) male and female BALB/c mice and C57BL/6 mice studied. (Sun et al, 2021)[21]	**Strain name:** MASCp36 - developed from MASCp6 (Gu et al, 2020)[6] **Dose:** Intranasal inoculation with varying doses including: 1.2 PFU, 12 PFU, 120 PFU, 1200 PFU, 12000 PFU **Shedding**: No information **Transmission**: No information	qRT-PCR results of aged BALB/c and C57BL/6 mice challenged with 12,000 PFU of MASCp36 showed that high levels of SARS-CoV-2 subgenomic RNAs were persistent in the lung and tracheas till 4 dpi. A similar tissue distribution of SARS-CoV-2 was observed in the young BALB/c and C57BL/6 mice.	**Clinical:** All the aged BALB/c and C57BL/6 mice challenged with high doses (1200 or 12,000 PFU) of MASCp36 developed typical respiratory symptoms and exhibited features like ruffled fur, hunched back, and reduced activity. Young BALB/c and C57BL/6 mice were resistant to MASCp36 challenge, and only one animal that received 12,000 PFU challenge died during the observation period. **Histopathological:** Necrotizing pneumonia and extensive diffuse alveolar damages observed on 4 dpi in aged mice. Milder pathology observed in the young mice.
Young adult (12 weeks old) and aged (One year old) BALB/c mice studied. (Dinnon et al, 2020)[7]	**Strain name:** IC-MA1 **Dose:** Intranasal inoculation with 10^5 PFU **Shedding**: No information **Transmission**: No information	High-titre virus replication was also observed in lung tissue at 2 dpi. This cleared by 4 dpi in the young adult mice but continued to persist at 4 dpi in the aged mice, suggesting that there was increased viral replication in the aged mice. MA1 was also observed in the upper airway and viral antigen was present in nasal turbinate epithelium at 2 dpi in young adult mice; viral antigen was found in conducting airway epithelium, interstitium and nasal epithelium in aged mice at 4 dpi.	**Clinical:** No overt clinical signs such as weight loss observed in young adult mice but a significant decrease in body weight was observed in aged mice. Whole-body plethysmography on mice indicated impaired lung function at 2 dpi, with the extent of impairment significantly worse in the aged mice. **Histopathological:** Interstitial congestion, epithelial damage, inflammatory infiltrate and peribronchial lymphocytic inflammation surrounding airways at 2 dpi. Histopathological effects seen in the aged mice are more severe than those observed in young adult mice.
Young (10-week-old) and aged (1 year old) BALB/c mice studied. (Leist et al, 2020)[8]	**Strain name:** IC-MA10 **Dose:** Doses ranging from 10^2, 10^3, 10^4 or 10^5 PFU were tested. However, 10^4 PFU and 10^3 PFU were determined as the optimal doses for analysis in young and aged mice respectively. **Shedding**: Both old and young mice exhibited viral titers in the nasal cavity over the first 3 days of infection. **Transmission**: No information	Virus replication in the lungs of young mice peaked 1–2 dpi and was absent in most surviving mice by 7 dpi. Viral replication in the upper respiratory tract of young mice remained high on 1–3 dpi but was undetectable in most mice by 5 dpi. A similar trend was observed in the aged mice, but the viral replication was detectable for a much longer period.	**Clinical**: Young mice rapidly lost weight and reached maximum weight loss at day 4 post inoculation. On day 5, the collective mortality rate was approximately 15%. Significant weight loss was also observed in aged mice. Mortality rates of 20% and 60% were recorded for infection with 10^4 and 10^5 PFU, respectively in the young mice. **Histopathological:** At the time of necropsy, acute stage lung damage was noted in the young mice. Analysis at 2, 4, and 7 dpi revealed early multifocal damage to conducting airway epithelia and hallmarks of diffuse alveolar damage (DAD) was observed. The aged mice had severe DAD and higher acute lung injury scores. Overall, a dose- and age-related increase in pathogenesis was observed.
C57Bl6, BALB/c and 129S1/SVMJ mice were studied Young (6-8-weeks) or aged (52 weeks old) C57Bl6 mice were used to study the effect of obesity, obesity-associated diabetes, and advanced age on clinical outcomes. (Rathnasinghe et al, 2021)[13]	**Strain name:** WA1-MA-P11 **Dose:** Intranasal inoculation with 2.5×10^4 PFU **Shedding**: No information **Transmission**: No information	Detectable virus titres in lungs and nasal turbinates of 129S1/SVMJ mice and lungs of male and female C57Bl6 and BALB/c mice, obtained at different days post infection	**Clinical:** Weight loss detected in the 129S1/SVMJ mice but not in the C57Bl6 and BALB/c mice. **Effect of increased age, comorbidities:** Both obesity/diabetes and advanced age in mice result in higher morbidity during SARS-CoV-2 infection.
Groups of young (4–6-week-old) female BALB/c mice, young (4–6-week-old female) C57BL/6J mice and aging (8–9-month-old) male BALB/c mice studied. (Wang et al, 2020)[23]	**Strain name:** HRB26M **Dose:** Intranasal inoculation with $10^{4.4}$ PFU in a volume of 50 µL. **Shedding**: No information **Transmission**: No direct evidence of transmission provided. However, the presence of efficient viral replication in the upper and lower respiratory tracts indicates that transmission could be possible.	In young BALB/c mice, viral RNA was detected in the nasal turbinates on day 3, 5, and 7 p.i. (post infection) and the infectious virus was detected on day 3 and 5 p.i. The viral RNA was also detected in the heart, liver, kidney, and spleen on day 3 p.i. In C57BL/6J mice, high viral loads in the nasal turbinates and lungs on days 3, 5 and 7 p.i. Similar observations made in the aging mice. However, when compared to the young mice, the average PFU titres in the aging mice were 3 times higher and 10 times higher in the nasal turbinates and lungs respectively.	**Clinical:** Similar to the young mice, the aging adult mice showed transient weight loss on days 2 and 3 p.i. and recovered thereafter. **Histopathological:** Mild pathological changes were observed in the respiratory tract of young BALB/c mice infected. Moderate-to-severe pathological changes in the lungs after infection in the aging mice.
Young (4–6-week-old) BALB/c mice studied. [Female 12-month-old BALB/c mice only used for the initial generation of the mouse adapted strain, not for any analysis of the mouse adapted strain]. (Huang et al, 2021)[26]	**Strain name:** Hu-1-WBP-1 **Dose:** Intranasally infected with 10-fold serial dilutions of the WBP-1 virus (i.e., 10^2 to 10^5 PFU). Subsequently, detailed analysis on mice was done by infecting mice with 50 µL of 2 LD_{50} [The LD_{50} of WBP-1 is $10^{3.8}$ PFU]. **Shedding:** No information **Transmission:** No information	In mice given the 50 µL of 2 LD_{50}: High viral loads were observed in the trachea and lung of infected mice, with lung tissues having the highest number of viral RNA copies. Trace amounts of viral nucleic acid were detectable in turbinate, heart, and spleen.	**Clinical**: In the groups of mice infected with the 10-fold serial dilutions: All groups of infected mice began to lose weight at 2 dpi and the weight loss was dose dependent. Bristled fur and depressed spirits in mice was also observed. The group of mice receiving a dose of 10^5 PFU WBP-1 virus all died (5/5) by 5 dpi. Two out of five mice survived in the group administered 10^4 PFU virus. In the mice given the 50 µL of 2 LD_{50}: Clinical signs of infection were observed in infected mice at 2 dpi. **Histopathological**: In mice given the 50 µL of 2 LD_{50}, Acute stage lung damage was noted. Moderate interstitial pneumonia with thickened alveolar septa occurred at 3 dpi, which progressed to severe interstitial pneumonia on 5 dpi. Inflammatory cell infiltration was observed in the lung tissue.
10-week-old female BALB/c mice). (Muruato et al, 2021)[27]	**Strain name:** IC-MA4 **Dose**: Mice infected with 10^5 PFU **Shedding:** No information **Transmission**: No information	Evidence of robust viral replication in mouse lungs.	**Clinical:** No information **Histopathological:** No information
10-week-old female BALB/c mice. (Muruato et al, 2021)[27]	**Strain name:** IC-CMA1, IC-CMA2, IC-CMA3 **Dose:** Mice intranasally inoculated with 10^5 PFU **Strain name:** IC-CMA3p20 [IC-CMA3 after passage 20] **Strain name:** IC-CMA3p20 [IC-CMA3 after passage 20] **Dose**: 10^5 PFU was the main dose administered, but doses 10^4 and 10^6 PFU also administered to some mice.	All three mutants (CMA1, CMA2, CMA3) produced approximately, 10^5 PFU per lobe at day 2 post infection. However, no virus was detected at day 4, suggesting rapid clearance by the host. In mice given IC-CMA3p20, robust viral replication was observed. There was a significantly greater viral load in the lung compared to IC-CMA3p20 at 2 dpi.	**Clinical:** None of the three mutants (CMA1, CMA2, CMA3) induced major disease, although both CMA2 and CMA3 caused more weight loss than CMA1. Mice infected with IC-CMA3p20 had a 10% weight loss by day 3 and showed signs of disease including ruffled fur and hunched posture. **Histopathological:** Mice infected with CMA3p20 had significant lung infiltration and inflammation characterized by peribronchiolar, perivascular cuffing, and perivasculitis by day 2 post infection. At 4 dpi, collapsed airways and interstitial pneumonia was observed in the mice.
Young (2 months old) and aged (12-month-old) BALB/c mice (Zhang et al, 2021)[28]	**Strain name:** LG **Dose**: 1×10^5 $TCID_{50}$ in a volume of 50 µl. **Shedding:** No transmission **Transmission:** No information	Effective viral replication in the lungs and trachea of the young and aged mice, although there was more viral replication in the aged mice.	**Clinical:** Weight of the aged mice was slightly decreased, but there were no evident changes in the weight of young mice. **Histopathological:** Lung lesions of the aged BALB/c mice were obvious, but those of young mice were not, with only slight lymphocyte exudation.

506

507
508 **Table 2.** Description of the characteristics of the mouse adapted strains generated from the *in vivo*
509 studies discussed in **Table 1**. *Strain = Mouse adapted strain name; Dose = Dose of SARS-CoV-2 mouse
510 adapted strain provided to the mice stated in plaque forming units (PFU) or the tissue culture infective
511 Dose (TCID50); Shedding & Transmission = Any evidence of viral shedding and viral transmission
512 observed in the mice.
513
514

	SARS-CoV-2 RBD mouse adaptations	human/mouse ACE2 interface residues within 5 Å of mutation
Region 1	**N501 Y**	38D/D, 41Y/Y, **353**K/H, 355D/D, 357R/R
	P499 T	41Y/Y, 45L/L, **329E/A**, 330N/N
	Q498 H/R/Y	41Y/Y, 42Q/Q, 45L/L, 49N/N, **61N/K**, 357R/R
Region 2	**Q493 K/R**	**34H/Q**, 35E/E, 38D/D, 42Q/Q
	K417 M/N/T	**31K/N**, **34H/Q**
Region 3	**E484 K/Q**	35E/E, 75E/E
	F486 L	75E/E, 76Q/Q, **78 T/K**, **79 L/T**, **82 M/S**

515

516

517

518 **Table 3.** SARS-CoV-2 spike RBD mutations associated with mouse adaptation and their close contact
519 residues in respective ACE2 proteins. Positions with dissimilar human/mouse residues are highlighted in
520 yellow.
521

522
523

	Essential position in RBD		Enhancing position(s) in RBD for mouse adaptation				
Analysis	Q498	N501	K417	E484	F486	Q493	P499
In silico [1]	H Y F W [5]	Y H F W [5]	N Q [8]	K Q	L	K L R	T
In vitro [2]	H Y F W	F Y V W T	-	R K T Q	-	M A Y F K L V	-
In vivo [3]	H R Y	Y	M N T	K Q	L	K R	T
In situ [4]	R H [6]	Y T H F [7]	N T M [9]	K Q R T [10]	L [11]	K L R [12]	T [13]

1. Predicted by our modelling. For E484, F486, Q493, and P499 our work only reconfirmed *in vivo* observations.

2. Arranged in descending order of affinity binding from *in vitro* experiments reported by Starr *et al.*[38]

3. Observed *in vivo* with studies summarized in Table 1 (alphabetical order). Note L486 and P499 were engineered.

4. Observed on GISAID as of 21 July 2021 after removing noise from low sample countries. Only key trends are presented.

5. These aromatic residues are predicted to have similar interactions with Y41 of ACE2.

6. F W Y not observed yet. Since early 2021, R observed in several countries, and H in Slovenia and USA (albeit the latter are of low quality and/or low coverage).

7. V W not observed yet. H observed in several countries (mid 2020), T in Spain's Canary Islands (early 2021), and F in Colombia, Germany, Mexico and Sweden (mid 2021). Y observed in several countries (**Figure S1**).

8. Modelled mutations predict favorable amide hydrogen bonding. N and Q mutations each require a single nucleotide change but there are 2 ways to get from N to K.

9. Q observed in the USA (August 2021). N (mutation G22813T) and T observed several countries (**Figures S2a** and **S2b**). Interestingly, N (alternative mutation G22813C) has a sporadic presence in UK and USA (since late 2020).

10. K observed in several countries (**Figure S2c**). Sporadic presence of Q (several countries from March 2020 to August 2021), R (Angola, Brazil, South Africa, South Korea, UK, USA, since late 2020), and T (USA in mid 2021) observed.

11. Sporadic presence of different synonymous mutations (T23018C in several countries; T23020G in

USA and one instance in Turkey) observed since late 2020.
12. A, F, M, V, Y not observed yet. Sporadic presence observed for K (Italy since early 2020), L (Trinidad and Tobago in mid 2021), and R (several countries mid 2020).
13. Sporadic presence since late 2020 in Bulgaria, Canada, Netherlands and USA.

Table 4. Comparison of *in silico*, *in vitro*, *in vivo* and *in situ* observations of key mutations in **Table 1**.

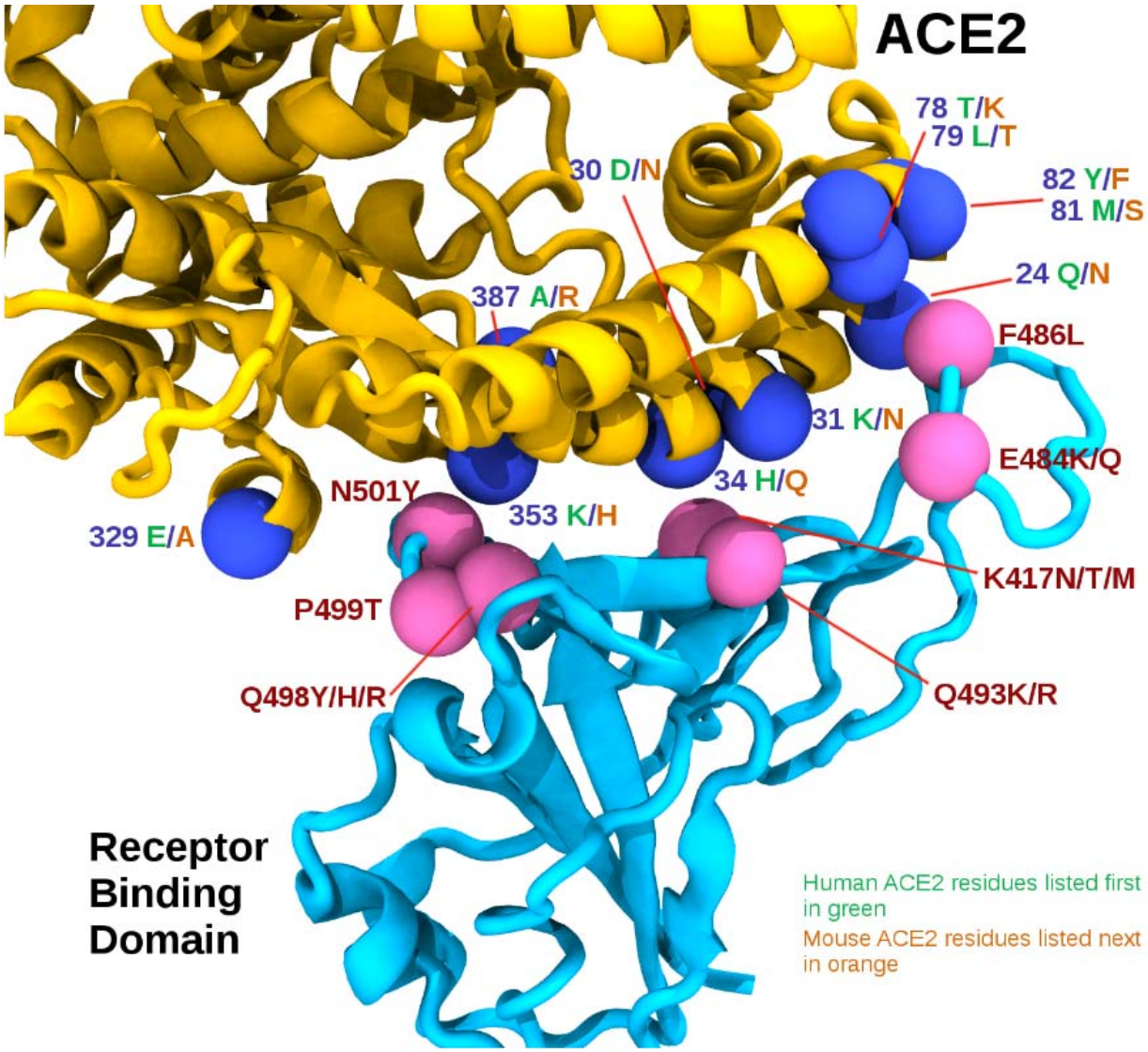

527

528 **Figure 1. The RBD/ACE2 interface.** The receptor binding domain (RBD) is shown in cyan, while the ACE2

529 is shown in yellow. Pink spheres indicate relative positions of mouse adapting mutations on the RBD,

530 while the blue spheres represent interface residues that differ between human and mouse ACE2

531 sequences, shown in green and orange respectively.

532

533

```
SP|Q9BYF1|ACE2_HUMAN MSSSSWLLLS LVAVTAAQST IEEQAKTFLD KFNHEAEDLF YQSSLASWNY NTNITEENVQ 60
SP|Q8R0I0|ACE2_MOUSE MSSSSWLLLS LVAVTTAQSL TEENAKTFLN NFNQEAEDLS YQSSLASWNY NTNITEENAQ 60
                     ********** *****:***   **:*****: :**:*****  ********** ********.*

SP|Q9BYF1|ACE2_HUMAN NMNNAGDKWS AFLKEQSTLA QMYPLQEIQN LTVKLQLQAL QQNGSSVLSE DKSKRLNTIL 120
SP|Q8R0I0|ACE2_MOUSE KMSEAAAKWS AFYEEQSKTA QSFSLQEIQT PIIKRQLQAL QQSGSSALSA DKNKQLNTIL 120
                     :*.:*. *** ** :***. * * : *****.   :* ***** **.***.**  **.*:*****

SP|Q9BYF1|ACE2_HUMAN NTMSTIYSTG KVCNPDNPQE CLLLEPGLNE IMANSLDYNE RLWAWESWRS EVGKQLRPLY 180
SP|Q8R0I0|ACE2_MOUSE NTMSTIYSTG KVCNPKNPQE CLLLEPGLDE IMATSTDYNS RLWAWEGWRA EVGKQLRPLY 180
                     ********** *****.**** ********:* ***.* ***. ******.**: **********

SP|Q9BYF1|ACE2_HUMAN EEYVVLKNEM ARANHYEDYG DYWRGDYEVN GVDGYDYSRG QLIEDVEHTF EEIKPLYEHL 240
SP|Q8R0I0|ACE2_MOUSE EEYVVLKNEM ARANNYNDYG DYWRGDYEAE GADGYNYNRN QLIEDVERTF AEIKPLYEHL 240
                     ********** ****:*:*** ********.: *.***:*.*. *******:**  *********

SP|Q9BYF1|ACE2_HUMAN HAYVRAKLMN AYPSYISPIG CLPAHLLGDM WGRFWTNLYS LTVPFGQKPN IDVTDAMVDQ 300
SP|Q8R0I0|ACE2_MOUSE HAYVRRKLMD TYPSYISPTG CLPAHLLGDM WGRFWTNLYP LTVPFAQKPN IDVTDAMMNQ 300
                     ***** ***: :******* * ********** *********  *****.**** *******::*
                                                |329                        |353
SP|Q9BYF1|ACE2_HUMAN AWDAQRIFKE AEKFFVSVGL PNMTQGFWEN SMLTDPGNVQ KAVCHPTAWD LGKGDFRILM 360
SP|Q8R0I0|ACE2_MOUSE GWDAERIFQE AEKFFVSVGL PHMTQGFWAN SMLTEPADGR KVVCHPTAWD LGHGDFRIKM 360
                     .***:***:* ********** *:****** * ****:*.: : *.******** **:***** *
                                                |387
SP|Q9BYF1|ACE2_HUMAN CTKVTMDDFL TAHHEMGHIQ YDMAYAAQPF LLRNGANEGF HEAVGEIMSL SAATPKHLKS 420
SP|Q8R0I0|ACE2_MOUSE CTKVTMDNFL TAHHEMGHIQ YDMAYARQPF LLRNGANEGF HEAVGEIMSL SAATPKHLKS 420
                     *******:** ********** ********* ********** ********** **********
```

534

535 **Figure 2** Sequence alignment of human and mouse ACE2 highlighting contact points with the SARS-

536 CoV-2 spike receptor binding domain in yellow. Differences between contact points are highlighted in

537 green (human) and orange (mouse), while common contact residues are highlighted in cyan.

538

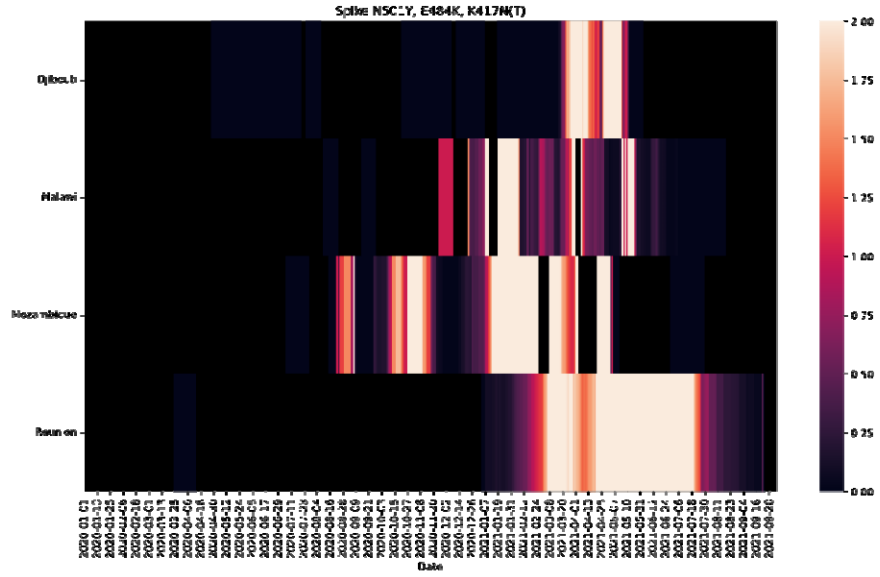

a)

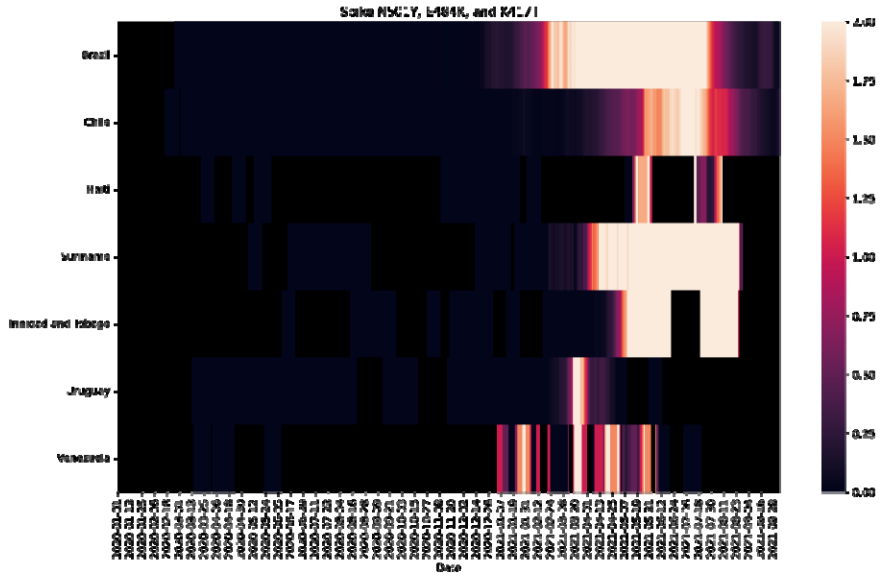

b)

Figure 3. Significant occurrences on GISAID of **a)** N501Y, E484K and K417N (nucleotide change G22813T) triple mutations and **b)** N501Y, E484K and K417T triple mutations, at the virus Receptor Binding Domain (RBD) since the start of the COVID-19 pandemic (31 December 2019). These countries are encouraged to perform targeted field surveillance.

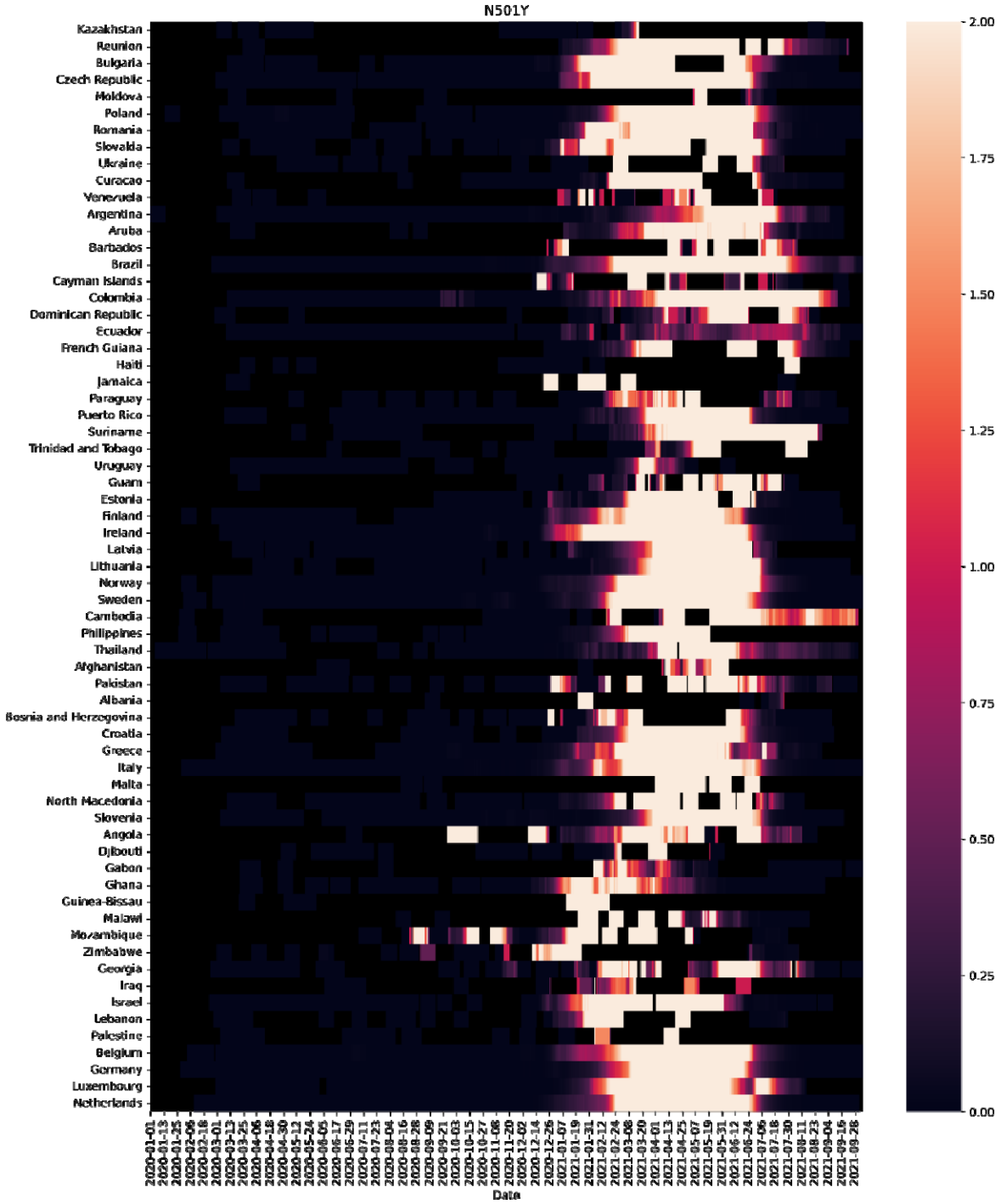

Figure S1. Significant occurrences on GISAID of the essential N501Y mutation (nucleotide change A23063T), at the virus Receptor Binding Domain (RBD) since the start of the COVID-19 pandemic (31 December 2019).

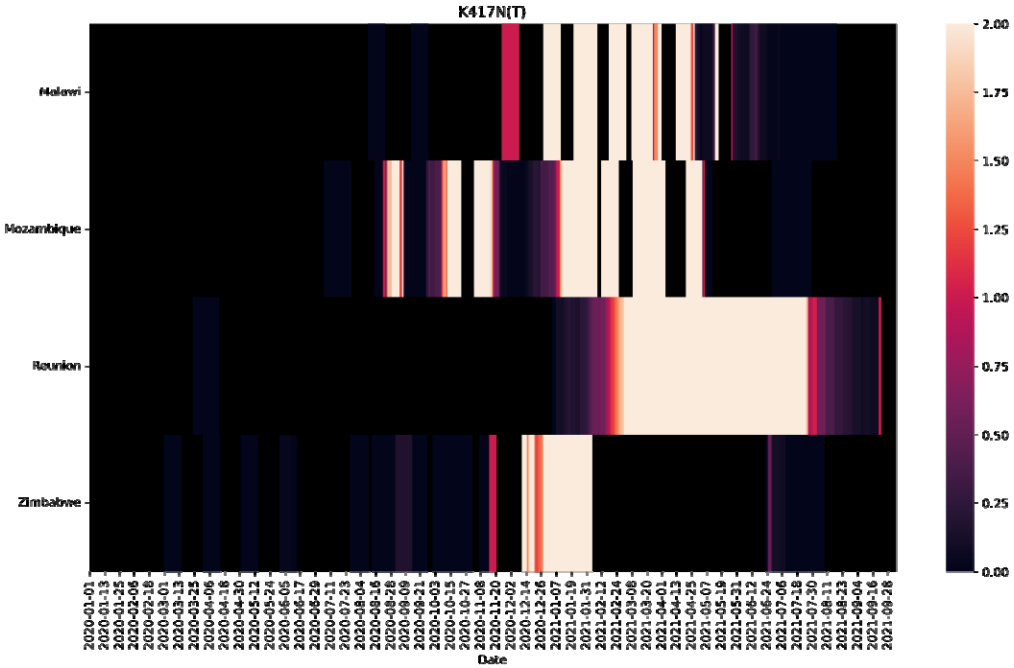
K417N(T)
Malawi
Mozambique
Reunion
Zimbabwe
Date
2.00
1.75
1.50
1.25
1.00
0.75
0.50
0.25
0.00

a)

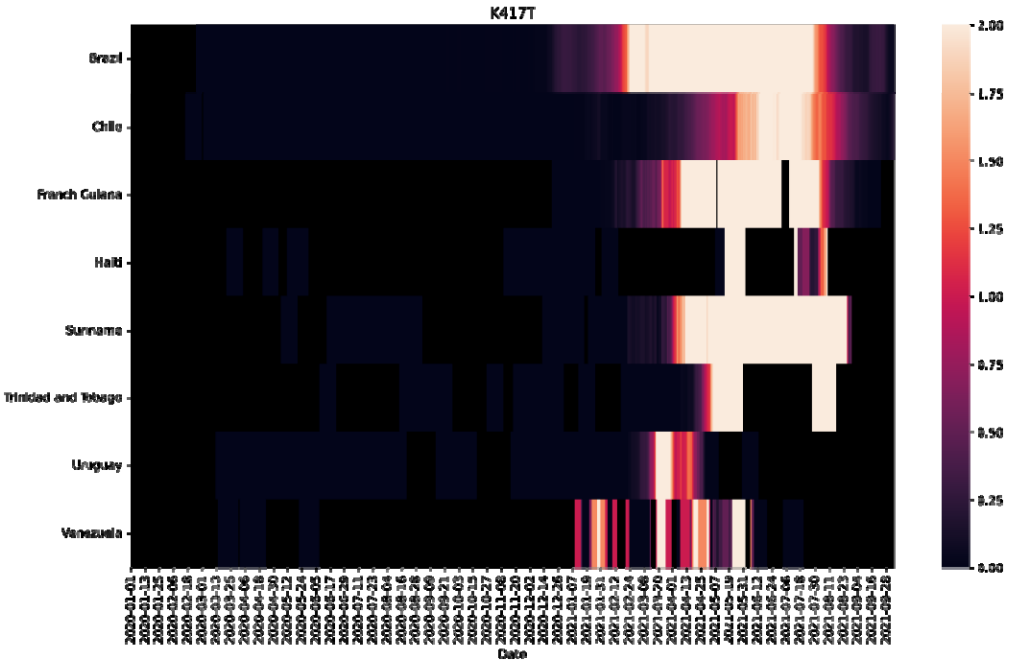
K417T
Brazil
Chile
French Guiana
Haiti
Suriname
Trinidad and Tobago
Uruguay
Venezuela
Date
2.00
1.75
1.50
1.25
1.00
0.75
0.50
0.25
0.00

b)

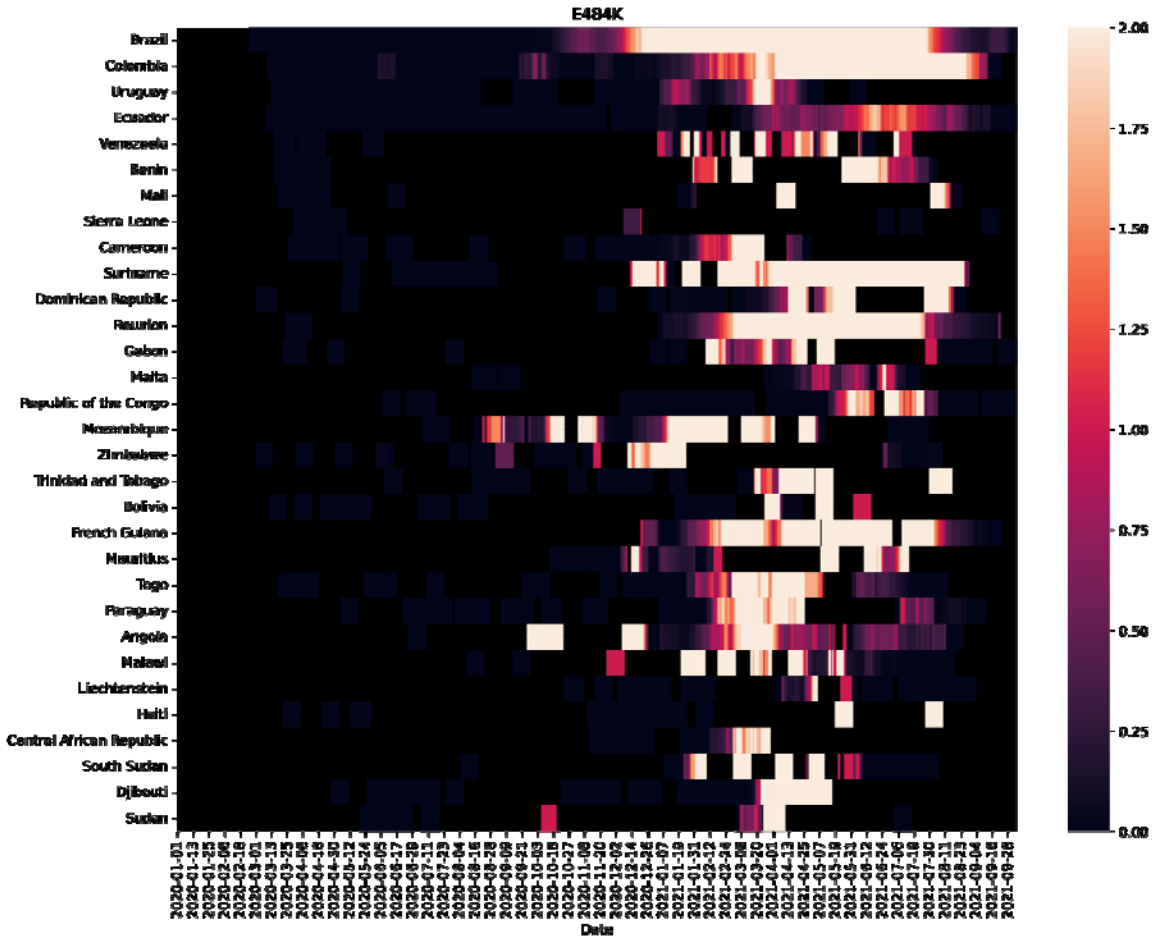

c)

Figure S2. Significant occurrences on GISAID of the enhancing mutations **a)** K417N (nucleotide change G22813T), **b)** K417T (nucleotide change A22812C), **c)** E484K (nucleotide change G23012A), at the virus Receptor Binding Domain (RBD), since the start of the COVID-19 pandemic (31 December 2019).

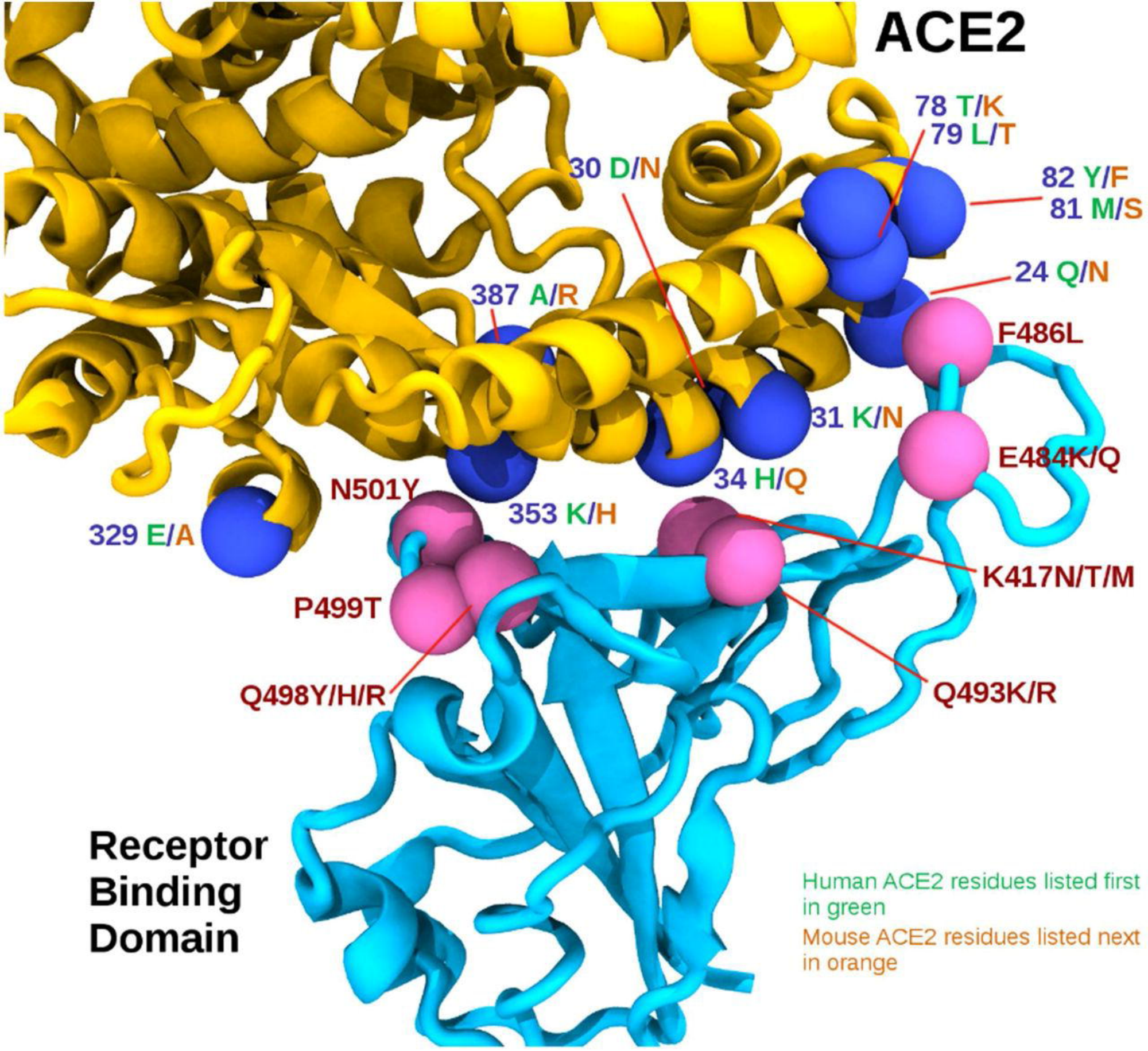
ACE2
78 T/K
79 L/T
30 D/N
82 Y/F
81 M/S
24 Q/N
387 A/R
F486L
31 K/N
E484K/Q
34 H/Q
N501Y
353 K/H
329 E/A
K417N/T/M
P499T
Q498Y/H/R
Q493K/R
Receptor Binding Domain
Human ACE2 residues listed first in green
Mouse ACE2 residues listed next in orange

```
SP|Q9BYF1|ACE2_HUMAN MSSSSWLLLS LVAVTAAQST IEEQAKTFLD KFNHEAEDLF YQSSLASWNY NTNITEENVQ 60
SP|Q8R0I0|ACE2_MOUSE MSSSSWLLLS LVAVTTAQSL TEENAKTFLN NFNQEAEDLS YQSSLASWNY NTNITEENAQ 60
                     ********** *****:***   **:*****: :**:***** **********  ********.*

SP|Q9BYF1|ACE2_HUMAN NMNNAGDKWS AFLKEQSTLA QMYPLQEIQN LTVKLQLQAL QQNGSSVLSE DKSKRLNTIL 120
SP|Q8R0I0|ACE2_MOUSE KMSEAAAKWS AFYEEQSKTA QSFSLQEIQT PIIKRQLQAL QQSGSSALSA DKNKQLNTIL 120
                     :*.:*. *** ** :***. * * : *****.   :* ***** **.***.**  **.*:*****

SP|Q9BYF1|ACE2_HUMAN NTMSTIYSTG KVCNPDNPQE CLLLEPGLNE IMANSLDYNE RLWAWESWRS EVGKQLRPLY 180
SP|Q8R0I0|ACE2_MOUSE NTMSTIYSTG KVCNPKNPQE CLLLEPGLDE IMATSTDYNS RLWAWEGWRA EVGKQLRPLY 180
                     ********** *****.**** ********:* ***.* ***. ******.**: **********

SP|Q9BYF1|ACE2_HUMAN EEYVVLKNEM ARANHYEDYG DYWRGDYEVN GVDGYDYSRG QLIEDVEHTF EEIKPLYEHL 240
SP|Q8R0I0|ACE2_MOUSE EEYVVLKNEM ARANNYNDYG DYWRGDYEAE GADGYNYNRN QLIEDVERTF AEIKPLYEHL 240
                     ********** ****:*:*** ********.: *.***:*.*. *******:**  *********

SP|Q9BYF1|ACE2_HUMAN HAYVRAKLMN AYPSYISPIG CLPAHLLGDM WGRFWTNLYS LTVPFGQKPN IDVTDAMVDQ 300
SP|Q8R0I0|ACE2_MOUSE HAYVRRKLMD TYPSYISPTG CLPAHLLGDM WGRFWTNLYP LTVPFAQKPN IDVTDAMMNQ 300
                     ***** ***: :******* * ********** *********  *****.**** *******::*
                                                |329                          |353
SP|Q9BYF1|ACE2_HUMAN AWDAQRIFKE AEKFFVSVGL PNMTQGFWEN SMLTDPGNVQ KAVCHPTAWD LGKGDFRILM 360
SP|Q8R0I0|ACE2_MOUSE GWDAERIFQE AEKFFVSVGL PHMTQGFWAN SMLTEPADGR KVVCHPTAWD LGHGDFRIKM 360
                     .***:***:* ********** *:****** * ****:*.: : *.******** **:****** *
                                                |387
SP|Q9BYF1|ACE2_HUMAN CTKVTMDDFL TAHHEMGHIQ YDMAYAAQPF LLRNGANEGF HEAVGEIMSL SAATPKHLKS 420
SP|Q8R0I0|ACE2_MOUSE CTKVTMDNFL TAHHEMGHIQ YDMAYARQPF LLRNGANEGF HEAVGEIMSL SAATPKHLKS 420
                     *******:** ********** ****** *** ********** ********** **********
```

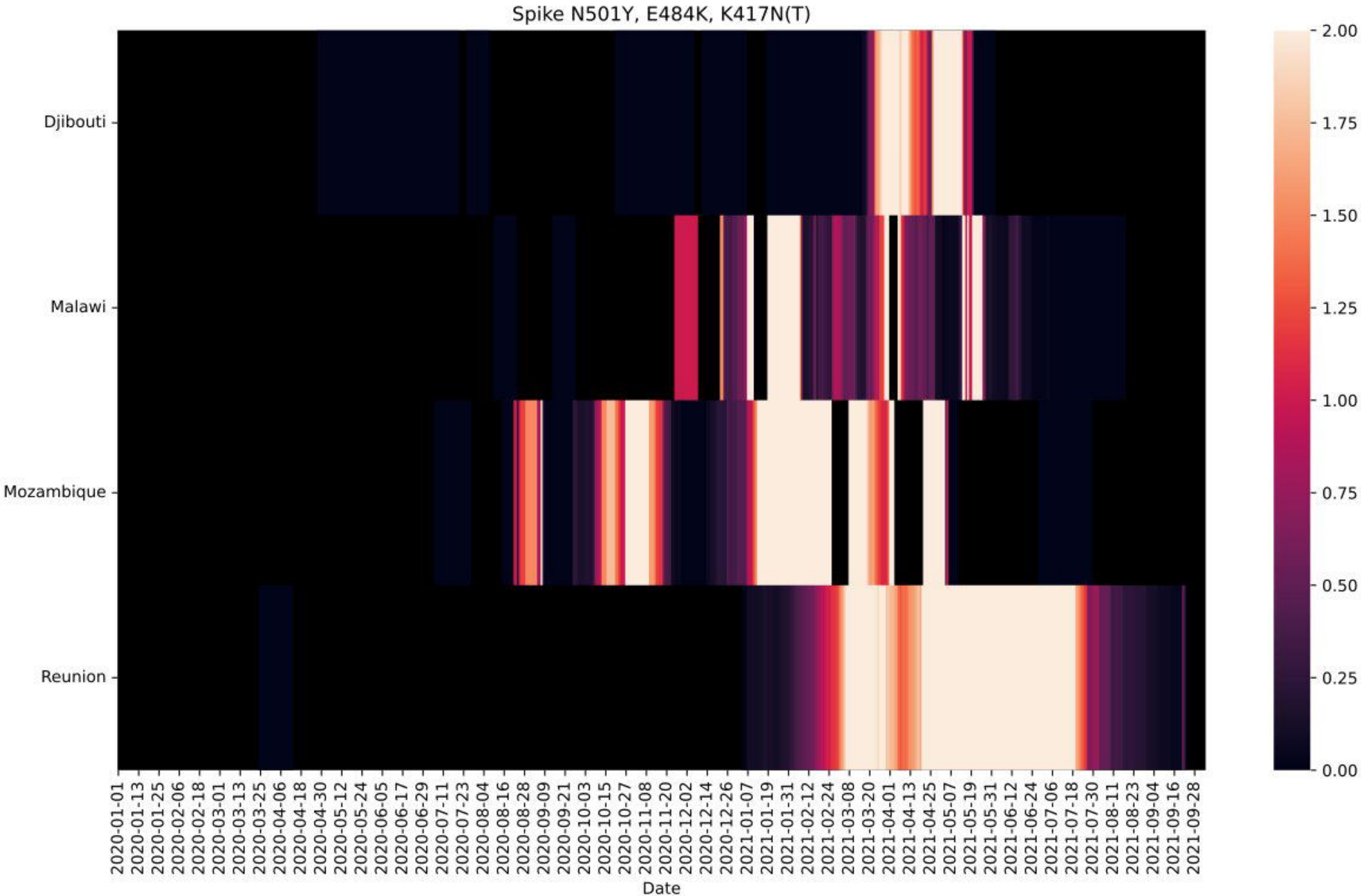
Spike N501Y, E484K, K417N(T)
Djibouti
Malawi
Mozambique
Reunion
2.00
1.75
1.50
1.25
1.00
0.75
0.50
0.25
0.00
2020-01-01
2020-01-13
2020-01-25
2020-02-06
2020-02-18
2020-03-01
2020-03-13
2020-03-25
2020-04-06
2020-04-18
2020-04-30
2020-05-12
2020-05-24
2020-06-05
2020-06-17
2020-06-29
2020-07-11
2020-07-23
2020-08-04
2020-08-16
2020-08-28
2020-09-09
2020-09-21
2020-10-03
2020-10-15
2020-10-27
2020-11-08
2020-11-20
2020-12-02
2020-12-14
2020-12-26
2021-01-07
2021-01-19
2021-01-31
2021-02-12
2021-02-24
2021-03-08
2021-03-20
2021-04-01
2021-04-13
2021-04-25
2021-05-07
2021-05-19
2021-05-31
2021-06-12
2021-06-24
2021-07-06
2021-07-18
2021-07-30
2021-08-11
2021-08-23
2021-09-04
2021-09-16
2021-09-28
Date

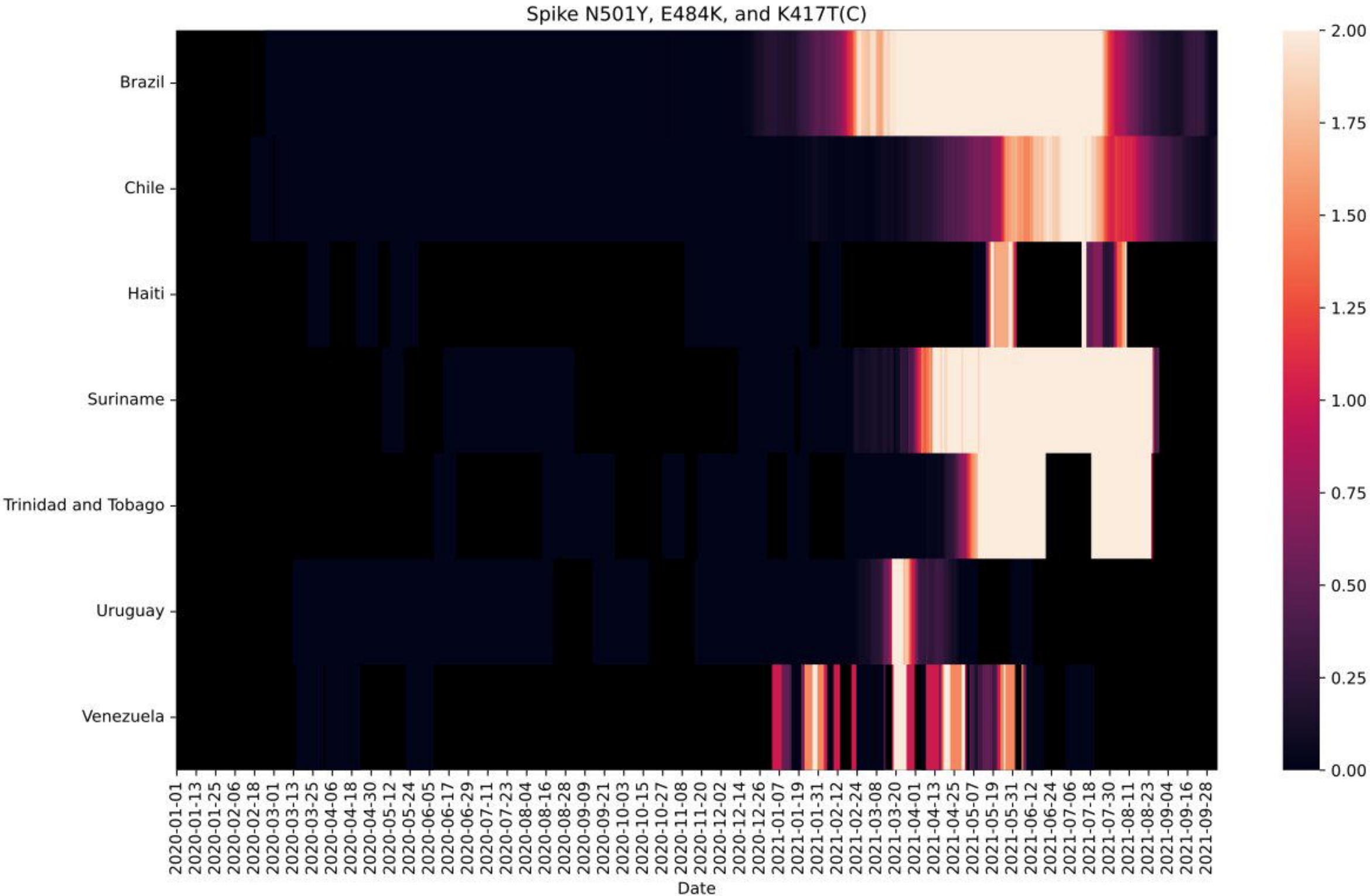
Spike N501Y, E484K, and K417T(C)
Brazil
Chile
Haiti
Suriname
Trinidad and Tobago
Uruguay
Venezuela
2020-01-01
2020-01-13
2020-01-25
2020-02-06
2020-02-18
2020-03-01
2020-03-13
2020-03-25
2020-04-06
2020-04-18
2020-04-30
2020-05-12
2020-05-24
2020-06-05
2020-06-17
2020-06-29
2020-07-11
2020-07-23
2020-08-04
2020-08-16
2020-08-28
2020-09-09
2020-09-21
2020-10-03
2020-10-15
2020-10-27
2020-11-08
2020-11-20
2020-12-02
2020-12-14
2020-12-26
2021-01-07
2021-01-19
2021-01-31
2021-02-12
2021-02-24
2021-03-08
2021-03-20
2021-04-01
2021-04-13
2021-04-25
2021-05-07
2021-05-19
2021-05-31
2021-06-12
2021-06-24
2021-07-06
2021-07-18
2021-07-30
2021-08-11
2021-08-23
2021-09-04
2021-09-16
2021-09-28
Date
2.00
1.75
1.50
1.25
1.00
0.75
0.50
0.25
0.00

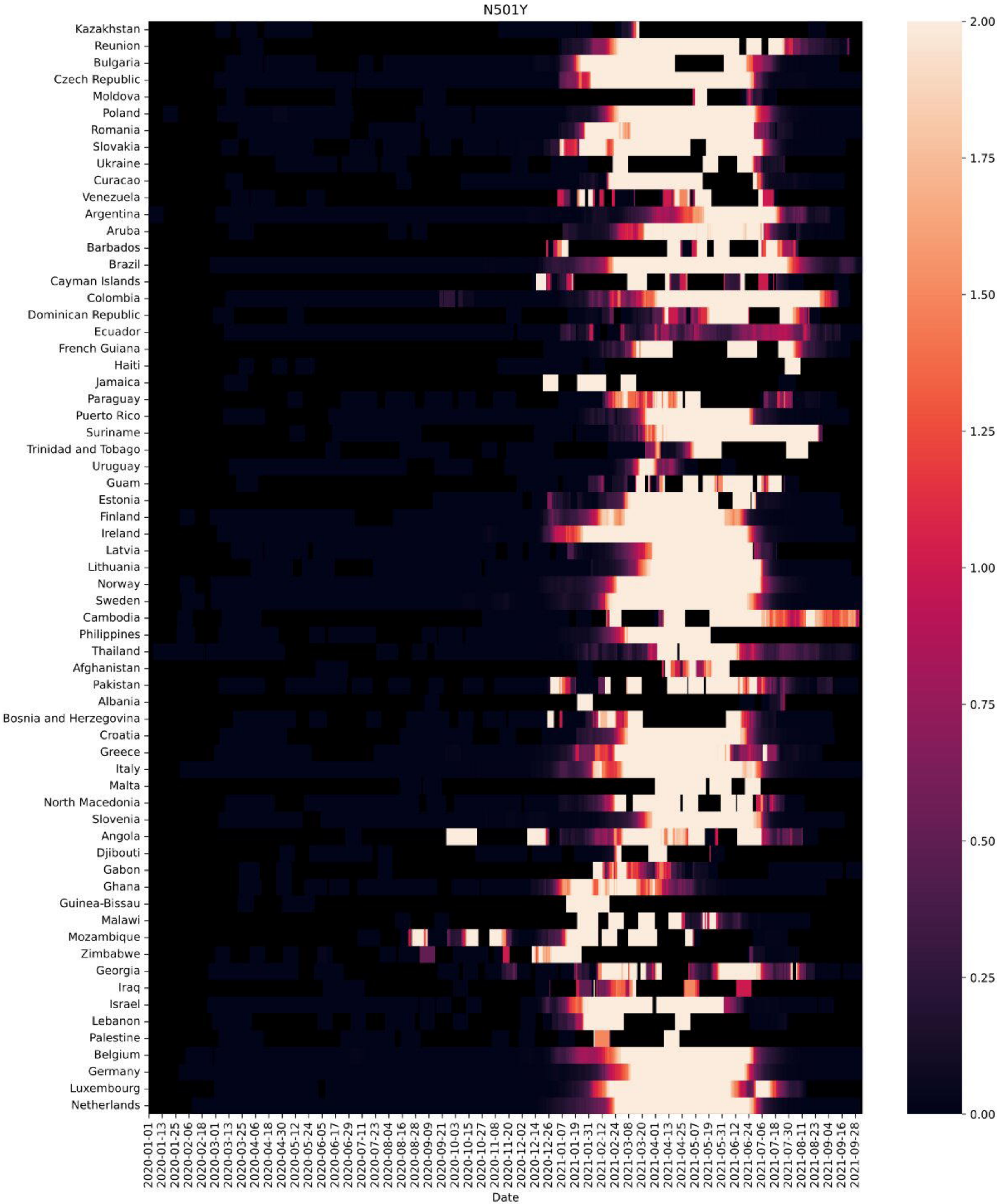
N501Y
Kazakhstan
Reunion
Bulgaria
Czech Republic
Moldova
Poland
Romania
Slovakia
Ukraine
Curacao
Venezuela
Argentina
Aruba
Barbados
Brazil
Cayman Islands
Colombia
Dominican Republic
Ecuador
French Guiana
Haiti
Jamaica
Paraguay
Puerto Rico
Suriname
Trinidad and Tobago
Uruguay
Guam
Estonia
Finland
Ireland
Latvia
Lithuania
Norway
Sweden
Cambodia
Philippines
Thailand
Afghanistan
Pakistan
Albania
Bosnia and Herzegovina
Croatia
Greece
Italy
Malta
North Macedonia
Slovenia
Angola
Djibouti
Gabon
Ghana
Guinea-Bissau
Malawi
Mozambique
Zimbabwe
Georgia
Iraq
Israel
Lebanon
Palestine
Belgium
Germany
Luxembourg
Netherlands
2020-01-01
2020-01-13
2020-01-25
2020-02-06
2020-02-18
2020-03-01
2020-03-13
2020-03-25
2020-04-06
2020-04-18
2020-04-30
2020-05-12
2020-05-24
2020-06-05
2020-06-17
2020-06-29
2020-07-11
2020-07-23
2020-08-04
2020-08-16
2020-08-28
2020-09-09
2020-09-21
2020-10-03
2020-10-15
2020-10-27
2020-11-08
2020-11-20
2020-12-02
2020-12-14
2020-12-26
2021-01-07
2021-01-19
2021-01-31
2021-02-12
2021-02-24
2021-03-08
2021-03-20
2021-04-01
2021-04-13
2021-04-25
2021-05-07
2021-05-19
2021-05-31
2021-06-12
2021-06-24
2021-07-06
2021-07-18
2021-07-30
2021-08-11
2021-08-23
2021-09-04
2021-09-16
2021-09-28
Date
2.00
1.75
1.50
1.25
1.00
0.75
0.50
0.25
0.00

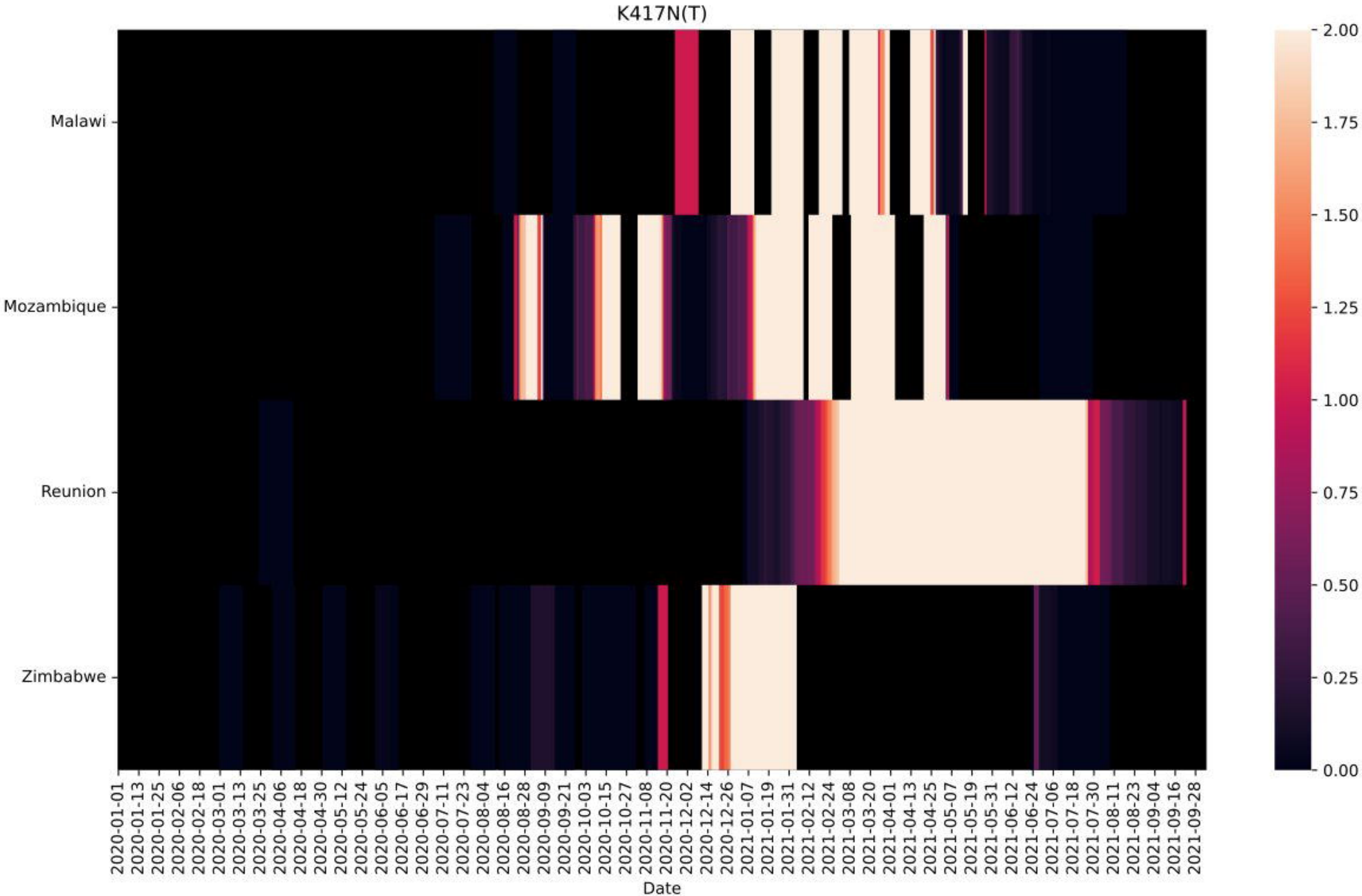
K417N(T)
Malawi
Mozambique
Reunion
Zimbabwe
2.00
1.75
1.50
1.25
1.00
0.75
0.50
0.25
0.00
2020-01-01
2020-01-13
2020-01-25
2020-02-06
2020-02-18
2020-03-01
2020-03-13
2020-03-25
2020-04-06
2020-04-18
2020-04-30
2020-05-12
2020-05-24
2020-06-05
2020-06-17
2020-06-29
2020-07-11
2020-07-23
2020-08-04
2020-08-16
2020-08-28
2020-09-09
2020-09-21
2020-10-03
2020-10-15
2020-10-27
2020-11-08
2020-11-20
2020-12-02
2020-12-14
2020-12-26
2021-01-07
2021-01-19
2021-01-31
2021-02-12
2021-02-24
2021-03-08
2021-03-20
2021-04-01
2021-04-13
2021-04-25
2021-05-07
2021-05-19
2021-05-31
2021-06-12
2021-06-24
2021-07-06
2021-07-18
2021-07-30
2021-08-11
2021-08-23
2021-09-04
2021-09-16
2021-09-28
Date

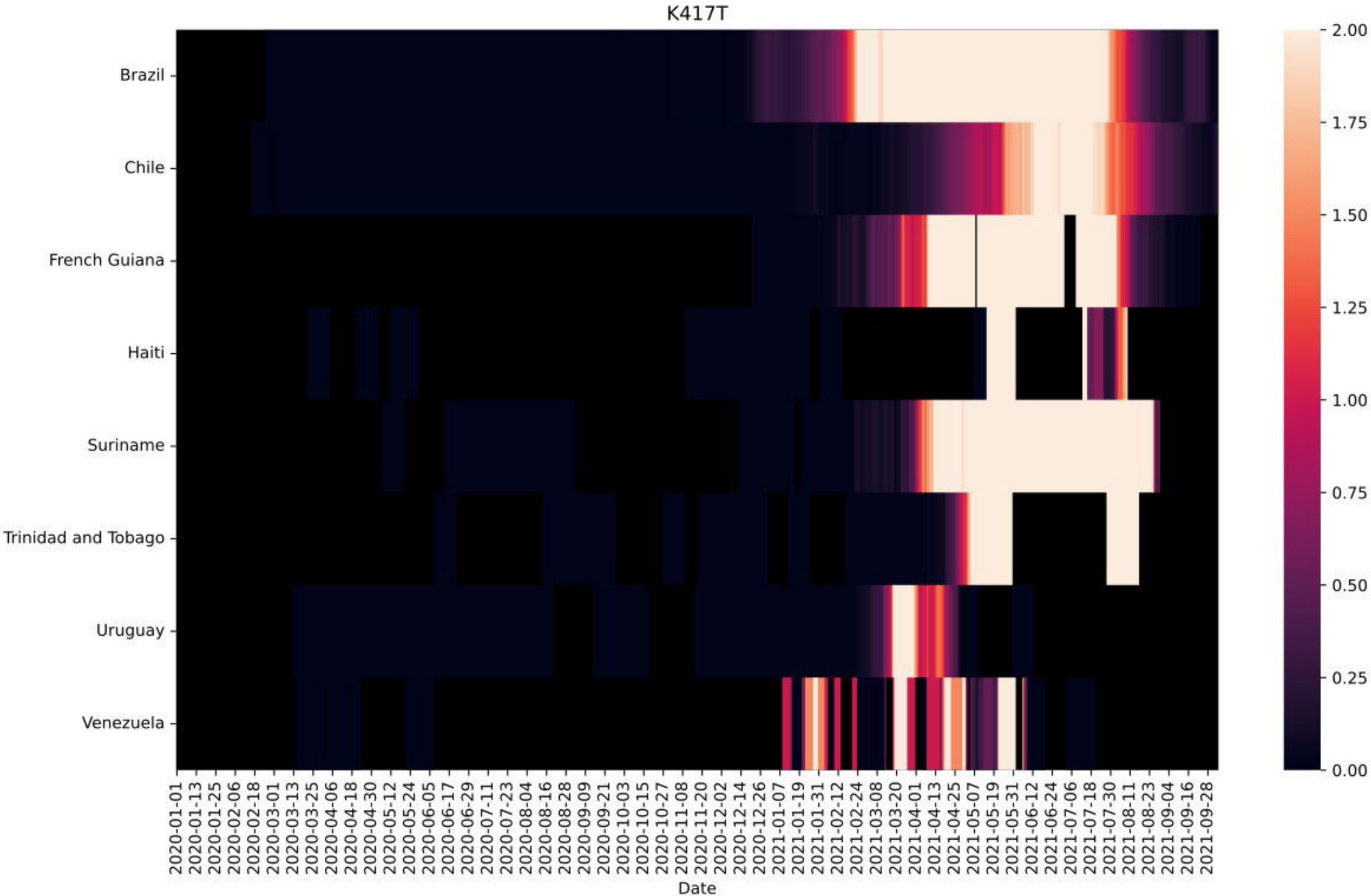
K417T
Brazil
Chile
French Guiana
Haiti
Suriname
Trinidad and Tobago
Uruguay
Venezuela
2020-01-01
2020-01-13
2020-01-25
2020-02-06
2020-02-18
2020-03-01
2020-03-13
2020-03-25
2020-04-06
2020-04-18
2020-04-30
2020-05-12
2020-05-24
2020-06-05
2020-06-17
2020-06-29
2020-07-11
2020-07-23
2020-08-04
2020-08-16
2020-08-28
2020-09-09
2020-09-21
2020-10-03
2020-10-15
2020-10-27
2020-11-08
2020-11-20
2020-12-02
2020-12-14
2020-12-26
2021-01-07
2021-01-19
2021-01-31
2021-02-12
2021-02-24
2021-03-08
2021-03-20
2021-04-01
2021-04-13
2021-04-25
2021-05-07
2021-05-19
2021-05-31
2021-06-12
2021-06-24
2021-07-06
2021-07-18
2021-07-30
2021-08-11
2021-08-23
2021-09-04
2021-09-16
2021-09-28
Date
2.00
1.75
1.50
1.25
1.00
0.75
0.50
0.25
0.00

E484K
Brazil
Colombia
Uruguay
Ecuador
Venezuela
Benin
Mali
Sierra Leone
Cameroon
Suriname
Dominican Republic
Reunion
Gabon
Malta
Republic of the Congo
Mozambique
Zimbabwe
Trinidad and Tobago
Bolivia
French Guiana
Mauritius
Togo
Paraguay
Angola
Malawi
Liechtenstein
Haiti
Central African Republic
South Sudan
Djibouti
Sudan
2020-01-01
2020-01-13
2020-01-25
2020-02-06
2020-02-18
2020-03-01
2020-03-13
2020-03-25
2020-04-06
2020-04-18
2020-04-30
2020-05-12
2020-05-24
2020-06-05
2020-06-17
2020-06-29
2020-07-11
2020-07-23
2020-08-04
2020-08-16
2020-08-28
2020-09-09
2020-09-21
2020-10-03
2020-10-15
2020-10-27
2020-11-08
2020-11-20
2020-12-02
2020-12-14
2020-12-26
2021-01-07
2021-01-19
2021-01-31
2021-02-12
2021-02-24
2021-03-08
2021-03-20
2021-04-01
2021-04-13
2021-04-25
2021-05-07
2021-05-19
2021-05-31
2021-06-12
2021-06-24
2021-07-06
2021-07-18
2021-07-30
2021-08-11
2021-08-23
2021-09-04
2021-09-16
2021-09-28
Date
2.00
1.75
1.50
1.25
1.00
0.75
0.50
0.25
0.00

Species and age of mice (Study reference)	Strain, dose, shedding and transmission*	Evidence of productive SARS-CoV-2 replication in the respiratory tract	Clinical outcomes, histopathological evidence of disease
Aged (9 months old) and young (6 weeks old) BALB/c mice studied. (Gu et al, 2020)[6]	**Strain name:** MASCp6 **Dose:** Intranasal inoculation with 1.6×10^4 PFU **Shedding**: Viral shedding observed in the feces at day 3,5 and 7 after inoculation. **Transmission**: No information	High amounts of viral RNAs in the lungs and tracheas were detected at 3, 5 and 7 days after inoculation in all aged mice, with peak viral RNA loads of ~10^{10} copies/g at 3 days after inoculation. Viral RNAs were also detected in heart, liver, spleen, and brain. Similar tissue distribution of SARS-CoV-2 RNA was also seen in the MASCp6 infected young mice.	**Clinical:** No visible clinical symptoms or body weight loss were observed in both the young and aged mice. No fatalities recorded. **Histopathological:** Led to interstitial pneumonia and inflammatory responses in both young and aged mice, however the lung damage in the aged mice was more severe.
Young (8-week-old) and aged (9 months old) male and female BALB/c mice and C57BL/6 mice studied. (Sun et al, 2021)[21]	**Strain name:** MASCp36 - developed from MASCp6 (Gu et al, 2020)[6] **Dose:** Intranasal inoculation with varying doses including: 1.2 PFU, 12 PFU, 120 PFU, 1200 PFU, 12000 PFU **Shedding**: No information **Transmission**: No information	qRT-PCR results of aged BALB/c and C57BL/6 mice challenged with 12,000 PFU of MASCp36 showed that high levels of SARS-CoV-2 subgenomic RNAs were persistent in the lung and tracheas till 4 dpi. A similar tissue distribution of SARS-CoV-2 was observed in the young BALB/c and C57BL/6 mice.	**Clinical:** All the aged BALB/c and C57BL/6 mice challenged with high doses (1200 or 12,000 PFU) of MASCp36 developed typical respiratory symptoms and exhibited features like ruffled fur, hunched back, and reduced activity. Young BALB/c and C57BL/6 mice were resistant to MASCp36 challenge, and only one animal that received 12,000 PFU challenge died during the observation period. **Histopathological:** Necrotizing pneumonia and extensive diffuse alveolar damages observed on 4 dpi in aged mice. Milder pathology observed in the young mice.
Young adult (12 weeks old) and aged (One year old) BALB/c mice studied. (Dinnon et al, 2020)[7]	**Strain name:** IC-MA1 **Dose:** Intranasal inoculation with 10^5 PFU **Shedding**: No information **Transmission**: No information	High-titre virus replication was also observed in lung tissue at 2 dpi. This cleared by 4 dpi in the young adult mice but continued to persist at 4 dpi in the aged mice, suggesting that there was increased viral replication in the aged mice. MA1 was also observed in the upper airway and viral antigen was present in nasal turbinate epithelium at 2 dpi in young adult mice; viral antigen was found in conducting airway epithelium, interstitium and nasal epithelium in aged mice at 4 dpi.	**Clinical:** No overt clinical signs such as weight loss observed in young adult mice but a significant decrease in body weight was observed in aged mice. Whole-body plethysmography on mice indicated impaired lung function at 2 dpi, with the extent of impairment significantly worse in the aged mice. **Histopathological:** Interstitial congestion, epithelial damage, inflammatory infiltrate and peribronchial lymphocytic inflammation surrounding airways at 2 dpi. Histopathological effects seen in the aged mice are more severe than those observed in young adult mice.
Young (10-week-old) and aged (1 year old) BALB/c mice studied. (Leist et al, 2020)[8]	**Strain name:** IC-MA10 **Dose:** Doses ranging from 10^2, 10^3, 10^4 or 10^5 PFU were tested. However, 10^4 PFU and 10^3 PFU were determined as the optimal doses for analysis in young and aged mice respectively. **Shedding**: Both old and young mice exhibited viral titers in the nasal cavity over the first 3 days of infection. **Transmission**: No information	Virus replication in the lungs of young mice peaked 1–2 dpi and was absent in most surviving mice by 7 dpi. Viral replication in the upper respiratory tract of young mice remained high on 1–3 dpi but was undetectable in most mice by 5 dpi. A similar trend was observed in the aged mice, but the viral replication was detectable for a much longer period.	**Clinical**: Young mice rapidly lost weight and reached maximum weight loss at day 4 post inoculation. On day 5, the collective mortality rate was approximately 15%. Significant weight loss was also observed in aged mice. Mortality rates of 20% and 60% were recorded for infection with 10^4 and 10^5 PFU, respectively in the young mice. **Histopathological:** At the time of necropsy, acute stage lung damage was noted in the young mice. Analysis at 2, 4, and 7 dpi revealed early multifocal damage to conducting airway epithelia and hallmarks of diffuse alveolar damage (DAD) was observed. The aged mice had severe DAD and higher acute lung injury scores. Overall, a dose- and age-related increase in pathogenesis was observed.
C57Bl6, BALB/c and 129S1/SVMJ mice were studied Young (6-8-weeks) or aged (52 weeks old) C57Bl6 mice were used to study the effect of obesity, obesity-associated diabetes, and advanced age on clinical outcomes. (Rathnasinghe et al, 2021)[13]	**Strain name:** WA1-MA-P11 **Dose:** Intranasal inoculation with 2.5×10^4 PFU **Shedding**: No information **Transmission**: No information	Detectable virus titres in lungs and nasal turbinates of 129S1/SVMJ mice and lungs of male and female C57Bl6 and BALB/c mice, obtained at different days post infection	**Clinical:** Weight loss detected in the 129S1/SVMJ mice but not in the C57Bl6 and BALB/c mice. **Effect of increased age, comorbidities:** Both obesity/diabetes and advanced age in mice result in higher morbidity during SARS-CoV-2 infection.
Groups of young (4–6-week-old) female BALB/c mice, young (4–6-week-old female) C57BL/6J mice and aging (8–9-month-old) male BALB/c mice studied. (Wang et al, 2020)[23]	**Strain name:** HRB26M **Dose:** Intranasal inoculation with $10^{4.4}$ PFU in a volume of 50 µL. **Shedding**: No information **Transmission**: No direct evidence of transmission provided. However, the presence of efficient viral replication in the upper and lower respiratory tracts indicates that transmission could be possible.	In young BALB/c mice, viral RNA was detected in the nasal turbinates on day 3, 5, and 7 p.i. (post infection) and the infectious virus was detected on day 3 and 5 p.i. The viral RNA was also detected in the heart, liver, kidney, and spleen on day 3 p.i. In C57BL/6J mice, high viral loads in the nasal turbinates and lungs on days 3, 5 and 7 p.i. Similar observations made in the aging mice. However, when compared to the young mice, the average PFU titres in the aging mice were 3 times higher and 10 times higher in the nasal turbinates and lungs respectively.	**Clinical:** Similar to the young mice, the aging adult mice showed transient weight loss on days 2 and 3 p.i. and recovered thereafter. **Histopathological:** Mild pathological changes were observed in the respiratory tract of young BALB/c mice infected. Moderate-to-severe pathological changes in the lungs after infection in the aging mice.
Young (4–6-week-old) BALB/c mice studied. [Female 12-month-old BALB/c mice only used for the initial generation of the mouse adapted strain, not for any analysis of the mouse adapted strain]. (Huang et al, 2021)[26]	**Strain name:** Hu-1-WBP-1 **Dose:** Intranasally infected with 10-fold serial dilutions of the WBP-1 virus (i.e., 10^2 to 10^5 PFU). Subsequently, detailed analysis on mice was done by infecting mice with 50 µL of 2 LD_{50} [The LD_{50} of WBP-1 is $10^{3.8}$ PFU]. **Shedding:** No information **Transmission:** No information	In mice given the 50 µL of 2 LD_{50}: High viral loads were observed in the trachea and lung of infected mice, with lung tissues having the highest number of viral RNA copies. Trace amounts of viral nucleic acid were detectable in turbinate, heart, and spleen.	**Clinical**: In the groups of mice infected with the 10-fold serial dilutions: All groups of infected mice began to lose weight at 2 dpi and the weight loss was dose dependent. Bristled fur and depressed spirits in mice was also observed. The group of mice receiving a dose of 10^5 PFU WBP-1 virus all died (5/5) by 5 dpi. Two out of five mice survived in the group administered 10^4 PFU virus. In the mice given the 50 µL of 2 LD_{50}: Clinical signs of infection were observed in infected mice at 2 dpi. **Histopathological**: In mice given the 50 µL of 2 LD_{50}, Acute stage lung damage was noted. Moderate interstitial pneumonia with thickened alveolar septa occurred at 3 dpi, which progressed to severe interstitial pneumonia on 5 dpi. Inflammatory cell infiltration was observed in the lung tissue.
10-week-old female BALB/c mice). (Muruato et al, 2021)[27]	**Strain name:** IC-MA4 **Dose**: Mice infected with 10^5 PFU **Shedding:** No information **Transmission**: No information	Evidence of robust viral replication in mouse lungs.	**Clinical:** No information **Histopathological:** No information
10-week-old female BALB/c mice. (Muruato et al, 2021)[27]	**Strain name:** IC-CMA1, IC-CMA2, IC-CMA3 **Dose:** Mice intranasally inoculated with 10^5 PFU **Strain name:** IC-CMA3p20 [IC-CMA3 after passage 20] **Strain name:** IC-CMA3p20 [IC-CMA3 after passage 20] **Dose**: 10^5 PFU was the main dose administered, but doses 10^4 and 10^6 PFU also administered to some mice.	All three mutants (CMA1, CMA2, CMA3) produced approximately, 10^5 PFU per lobe at day 2 post infection. However, no virus was detected at day 4, suggesting rapid clearance by the host. In mice given IC-CMA3p20, robust viral replication was observed. There was a significantly greater viral load in the lung compared to IC-CMA3p20 at 2 dpi.	**Clinical:** None of the three mutants (CMA1, CMA2, CMA3) induced major disease, although both CMA2 and CMA3 caused more weight loss than CMA1. Mice infected with IC-CMA3p20 had a 10% weight loss by day 3 and showed signs of disease including ruffled fur and hunched posture. **Histopathological:** Mice infected with CMA3p20 had significant lung infiltration and inflammation characterized by peribronchiolar, perivascular cuffing, and perivasculitis by day 2 post infection. At 4 dpi, collapsed airways and interstitial pneumonia was observed in the mice.
Young (2 months old) and aged (12-month-old) BALB/c mice (Zhang et al, 2021)[28]	**Strain name:** LG **Dose**: 1×10^5 $TCID_{50}$ in a volume of 50 µl. **Shedding:** No transmission **Transmission:** No information	Effective viral replication in the lungs and trachea of the young and aged mice, although there was more viral replication in the aged mice.	**Clinical:** Weight of the aged mice was slightly decreased, but there were no evident changes in the weight of young mice. **Histopathological:** Lung lesions of the aged BALB/c mice were obvious, but those of young mice were not, with only slight lymphocyte exudation.